Multi-functional fluorinated $NiTiO_3$ perovskites for CO_2 photocatalytic reduction, electrocatalytic water splitting, and biomedical waste management

E.A. Dawi[1], M. Padervand[2*], S. Ghasemi[3*], S. Hajiahmadi[4], K. Kakaei[2], Z. Shahsavari[4], S. Karima[4], M. Baghernejad[5], M. Signoretto[6], Z. H. Ibupoto[7], A. Tahira[8], and C. Wang[9*]

[1]Nonlinear Dynamics Research Center (NDRC), Ajman University, Ajman, P.O. Box 346, United Arab Emirates.

[2]Department of Chemistry, Faculty of Science, University of Maragheh, P.O Box 55181-83111, Maragheh, Iran.

[3]Sharif Energy, Water, and Environment Institute, Sharif University of Technology, Azadi Avenue, PO Box 11365-8639, Tehran, Iran.

[4]Department of Clinical Biochemistry, Shahid Beheshti University of Medical Sciences, P. O. Box 19615-1178, Tehran, Iran.

[5]Helmholtz-Institute Münster, IEK-12, Forschungszentrum Jülich GmbH, Corrensstraße 46, Münster 48149, Germany.

[6]CATMAT Lab, Department of Molecular Sciences and Nanosystems Ca' Foscari University Venice and INSTM Consortium, RU of Venice, Via Torino 155, 30172 Venezia Mestre, Italy.

[7]Dr. M.A Kazi Institute of Chemistry University of Sindh, Jamshoro, 76080, Pakistan.

[8]Institute of Chemistry, Shah Abdul Latif University Khairpur Mirs, Sindh, Pakistan.

[9]School of Environmental Science and Engineering, Shaanxi University of Science and Technology, Xi'an 710021, China.

*Corresponding authors: Email: padervand@maragheh.ac.ir (M. Padervand), Tell: +98 41 37278001, sh.ghasemi@sharif.edu (S. Ghasemi), Tell: +98 21 66085185, wangchuanyi@sust.edu.cn (C. Wang), Tell: +86-13299131206

Abstract

Multi-functional F-doped $NiTiO_3$ structures with high stability were prepared by a template-free hydrothermal method. A multi-technique approach including several physicochemical techniques was employed to describe the morphology, electronic properties, and structural characters. The F-doped $NiTiO_3$ catalyst showed a much higher CO_2 to CH_4 photocatalytic conversion rate (2.6 μmol g^{-1} h^{-1}) than pristine $NiTiO_3$ (1.6 μmol

g^{-1} h^{-1}), highlighting the key role of F impurities in suppressing the charge carriers recombination. In addition to the higher efficiency and reusability than Pt/C reference electrode towards electrocatalytic water splitting, a lower Tafel slope was recorded for the F-doped structure (81.2 mV dec^{-1}). This implies significant improvement in the reaction kinetics, arising from the synergistic effects between the F sites and bulk constituents to supply more desired active electronic states. The capability of the structures for the biomedical wastewater (containing the Caco-2 cancer cells) treatment was also explored. According to several biochemical assays, the fluorinated material shows a promising performance against the tumor cells at its IC50 concentration, 0.15 μg/mL, in a typical hospital wastewater. Our results pave the way for developing novel multi-functional photoactive titanate perovskites aiming at future clean energy transition.

Keywords: $NiTiO_3$; Fluorine doping, CO_2 reduction; Biomedical wastewater; Electrocatalytic water splitting

1. Introduction

Titanate perovskites are a well-known family of photoactive inorganic materials with the chemical formula $ATiO_3$, in which A is a rare or alkaline earth element. The mechanical resistance of titanate perovskites is mainly governed by the type of A element in the formula, while practical catalytic and electronic applications are granted by the titanium part of the material [1]. Titanate perovskites have frontier d-orbitals that are energetically similar to O2p orbitals. Because of this energy proximity, the Ti d-orbitals and O2p orbitals have strong interactions, leading to significant orbital hybridization. This hybridization plays a crucial role in determining the electronic structure of these materials, particularly in the vicinity of the Fermi level. The orbital's hybridization,

therefore, dominates the electronic structure of these titanate perovskites near the Fermi level. The topmost valence band(VB) in titanate perovskites consists of O2p orbitals. These orbitals are responsible for bonding oxygen and titanium ions in the perovskite lattice. Hybridization of the O2p and Ti d-orbitals affects the electronic properties at the maximum of the valence band. Alternatively, the d-orbitals of titanium metal form the bottommost conduction band(CB) in titanate perovskites. As a result of their higher energy than the O2p orbitals, these d-orbitals enable electron delocalization, allowing electrical conduction to occur. The composition and structure of titanate perovskites determine the specific conduction band characteristics. Titanate perovskites possess a high band gap energy, typically broader than 3.00 eV. The wide band gap in titanate perovskites makes them interesting for various applications, such as dielectric materials, photocatalysis, and energy storage devices. The electronic structure, particularly the orbital hybridization and the energy positioning of the valence and conduction bands is critical for understanding and optimizing the properties of these materials for specific applications. Accordingly, a large variety of these materials, such as zinc titanates [2, 3], nickel titanates [4-7], iron titanates [8, 9], strontium titanates [10, 11], and barium titanates [12, 13] have been recently explored to address the energy and environmental concerns. The octahedral lattice of perovskite structures facilitates the mobility of electrons and oxygen deficiencies throughout the structure [14], leading to higher charge separation efficiency in light-driven catalysis. Furthermore, their narrow bandgaps improve titanate perovskites' photo-catalytic performance [15]. To ameliorate the light-harvesting properties of aforementioned titanates, researchers investigated several approaches, among which doping non-metals, such as nitrogen [16, 17], fluorine [18], and phosphorous [19] and inducing lattice defects [20, 21] proved to be effective. Suitable metal or non-metal dopants not only adjust the electronic concentration, mobility, and

lifetime of the charge carriers but also effectively produces doping-induced states with localized or delocalized nature between the VB and the CB that affects the electronic and optical properties, causing the bandgap energy reduction, thereby leading to more noticeable charging absorption. On the other hand, metal or nonmetal dopants can act as a sinker of photogenerated e^-/h^+ pairs in the titania lattice, facilitating charge separation and diminishing their recombination. Dopants may substitutionally locate in Ti(IV) lattice positions and/or located at interstitial sites. Donor levels are created above the valence band maximum (VBM), while, acceptor levels are formed below the conduction band minimum (CBM), thus inducing visible light absorption and improving activity under visible light irradiation. Besides, the intermediate band or mid-gap state in the middle of the band gap formed by delocalized states band can be achieved with heavy dopants, promoting charge transport and photoconductivity [22-24]. Moreover, despite its complexity, imposing metal defects at the surface of the lattice is proven to be an effective strategy to bring a synergetic effect to boost the perovskite photoactivity [25, 26]. In fact, vacancies in bulk can act as electron-hole recombination centers decreasing the photo-catalytic performance [27].

Optimizing the synthesis conditions should be explicitly considered to reach a desired morphology and size distribution pattern besides ameliorated optoelectronic properties and optimum materials stability [28]. In this regard, several shapes of titanate perovskite particles have been synthesized and proven with improved light sorption capacity and photocatalytic performance. Examples include regular polyhedrons [29, 30], irregular particles [28, 31], rod-like [32, 33], spherical [34], tubular [35], and fibers [36]. Accordingly, many strategies have been discussed for the successful fabrication of titanate perovskites with promising photoactivity, among which hydrothermal, solvothermal, electrospinning, sol-gel, and solid-state pyrolysis have been well verified

[30].

Perovskite applications are beyond energy conversion and can be employed for the photodegradation of organic pollutants such as dye compounds[37-41], herbicides [42], antibiotics [43], and microbial contaminants [44]. Additionally, these structures are proven to enable photo-catalytic conversion of gaseous pollutants from industrial and domestic sources, including NOx compounds [45-47] and CO_2 [48, 49]. These hazards adversely affect the quality of animate life and ecosystems irretrievably [50, 51]. Several titanate perovskite-based photocatalysts, including $SrTiO_3$ [52-55], $FeTiO_3$ [56-58], $BaTiO_3$ [48, 59-61], $ZnTiO_3$ [62], and $NiTiO_3$ [63-66], with a variety of doped impurities and morphologies, have been reported for the CO_2 and NOx photoconversion. To the best of our knowledge, the performance of F-doped nickel titanate structures toward CO_2 photo-catalytic reduction has not yet been investigated.

Herein, firstly, successful hydrothermal synthesis of novel octahedral carbonized F-doped $NiTiO_3$ photocatalysts is reported, and the morphological and structural properties are analyzed to comprehensively characterize the material's properties using a multi-technique approach, including several physical-chemical methods. Second, this work investigates the newly synthesized F-doped $NiTiO_3$ photoactive structures toward heterogeneous gas-phase CO_2 reduction reaction to methane. As another application, it is shown that the titanate perovskite offers superior electrocatalytic potential for the oxygen evolution reaction (OER) and oxygen reduction reaction (ORR) through water splitting for clean energy production from water splitting reactions [67]. Compared to the reference commercial electrocatalyst like Pt/C, several metal-doped electrocatalysts [68-70] and heterojunction structures [5, 71] of titanate perovskites have been reported to enhance the electrocatalytic yield. Still, the structural stability of such materials remains a big challenge. To address this issue, the growth of electrocatalytic $NiTiO_3$ on various

supports, such as Volcan C [72], reduced graphene [5], P25 TiO_2 [73], and active carbon [74], LDHs [75], has been considered. However, no study has been reported on the effect of F-doping on improving the electrocatalytic performance and structural stability of nickel titanate perovskite.

As another application of such novel structure, this work investigates the F-doped $NiTiO_3$ structures to potentially treat biological wastes, which has been extensively addressed in the past decade [76]. Annually, a considerable amount of liquid effluents from the as-related processes releases to the ecosystem, among which cancer cell samples are one of the undesirable ingredients [77]. Although conventional *in vitro* and *in vivo* cell treatment methods, e.g., ozonation, chlorination, flocculation, electrochemical equipment, and UV disinfection, can be used towards these goals, due to the drawbacks such as secondary pollution generation, recolonization, and high energy consumption, they have not gained widespread application for such contaminants yet. Instead, a large variety of nanostructured materials, including silica-based nanocomposites [36], magnetic nanoparticles [78, 79], carbon nanotubes [80], noble metal nanoparticles [81], quantum dots (QDs) [82], and semiconducting nanostructures[83, 84] have been investigated to minimize the risks of aforementioned biohazards through removing contaminants via adsorption and degradation[79, 85]. As an eco-friendly technology, photocatalysis has been strongly recommended for disinfecting many bio-pollutants at ambient conditions. Some advantages of photocatalysis technology, such as versatility, efficiency, non-selective action, lack of chemical additions, reusability, low operating costs, depreciation of byproducts, and scalability, make them comparable to other water treatment strategies. It is important to note that the effectiveness of photocatalysis can be influenced by various factors, such as the type and concentration of contaminants, water quality parameters, and the choice of the photocatalyst. Overall, the unique

combination of advanced oxidation capabilities, broad-spectrum activity, pathogen inactivation, sustainability, and potential for decentralized applications makes photocatalysis a distinctive and promising approach for wastewater treatment [86]. Defective TiO_2-based semiconductors [87, 88], polyoxometalate-contained composites [48], polymeric C_3N_4-based nanostructures [89], carbon QDs-based photocatalysts [61, 90], WO_3-based nanoparticles [91, 92], and plasmonic $ZnTiO_3$ nanomaterials [62] have recently shown superb potential of removing cancer cells waste under visible light. Here, we discuss the novel and efficient photo-catalytic remediation of cancer cell wastewater over the F-doped titanate perovskite structure.

To summarize, the photoactivity of the synthesized structures is explored for visible-light-driven CO_2 photoreduction in the presence of water vapor and electrocatalytic water splitting. Anticancer properties of the photocatalysts are also investigated against Caco-2 cancer cells (as a typical biomedical wastewater sample). The mechanism of action is well discussed based on several biochemical assays and fluorescence microscopy images.

2. Materials and Methods

2.1 Reagents

Nickel (II) nitrate hexahydrate, ethylene glycol, hydrogen peroxide 30%, nitric acid 65%, and sodium fluoride were purchased from Merck and used as received. Potassium titanium oxalate, from Sigma Aldrich, was also used as the Ti precursor.

To perform the biochemical experiments, high glucose medium culture (DMEM), antibiotics (penicillin and streptomycin), and de-attaching enzyme (Trypsin/EDTA) were purchased from Gibco (Germany). The MTT dye (3-(4, 5-dimethylthiazol-2-yl)-2, 5-diphenyltetrazolium bromide) was supplied by Sigma-Aldrich (Munich, Germany). Cayman Chemical Co. provided the caspase 3/7 ELISA assay kit, JC-1 Mitochondria Membrane Potential Assay kit, and ROS detection cell-based assay kit.

2.2 Materials Synthesis

Carbonized pristine $NiTiO_3$ was prepared according to the following procedure: the equimolar amounts of Ti and Ni sources were respectively dissolved in 80 mL of ethylene glycol with heating. Hydrogen peroxide and diluted nitric acid solution were then added to the ethylene glycol solution drop by drop under magnetic stirring. After 2h of stirring, the mixture was poured into a 200 mL stainless steel autoclave. The autoclave was transferred to an oven and kept at 423 K for 18 h. After the hydrothermal treatment, the obtained residue was repeatedly washed with deionized water and ethanol and dried at 338 K.

The procedure was repeated to synthesize the octahedral F-doped $NiTiO_3$/C microparticles. At the same time, sodium fluoride, 0.04 mol, was added to the ethylene glycol solution containing Ti and Ni sources before hydrothermal treatment. All the other steps were similarly conducted without further alterations in the condition.

2.3 Materials Characterization

The morphological properties of the photocatalysts were characterized by Field Emission Scanning Electron Microscopy (FESEM, XL30 model coupled with the EDX system) and Transmission Electron Microscopy (TEM, FEI Tecnai G2 f20 s-twin with an acceleration voltage of 200 kV). The crystalline phases were identified by X-ray diffraction (XRD, Bruker D8 Advance diffractometer with Cu Kα radiation, $\lambda = 0.15406$ nm). X-ray photoelectron spectroscopy (XPS, a Shimadzu-Amics instrument with aluminum Ka radiation) was performed to describe the chemical composition of as-prepared materials. Fourier transform infrared (FT-IR) spectra in the 4000–400 cm^{-1} range were recorded on a Bruker Vertex 70 spectrophotometer. The Raman and UV–visible diffuse reflectance spectra were recorded on a Dispersive Raman microscopy with a 785 nm laser and a UV–visible spectrophotometer (Shimadzu Solidspec−3700 DUV, $BaSO_4$ as the reference standard), respectively. Electron paramagnetic resonance (EPR) was performed on a

Bruker E500 instrument equipped with an Oxford cryostat performing under the X-band at 100 K.

2.4 Photo-catalytic Experiments

2.4.1 CO_2-to-CH_4 photoreduction

The CO_2 photoreduction tests were conducted using 20 mg of the photocatalyst powder and 2 mL deionized water in a 50 mL reactor. High-purity carbon dioxide gas was purged into the reactor, illuminated by a 300 W Xe lamp equipped with a 420 nm cutoff filter to provide the visible light photons. The reactor temperature was kept at 293 K under magnetic stirring during the reaction time. The concentration of the products was analyzed using Agilent 7890 B gas chromatography.

2.4.2 Electrocatalytic experiments

Electrochemical measurements were carried out on VSP300, biologic Inc. using a standard three-electrode setup in a 1 M KOH electrolyte solution with a Pt wire as the counter electrode, an Ag/AgCl electrode as the reference electrode, and a glassy carbon electrode (GCE) with a geometric area of 0.042 cm^2 as the working electrode. 5 mg of each catalyst and 10 µL of Nafion were ultrasonically dispersed in 1 mL of water/alcohol (v/v 3: 1) combination solution for 25 min. 5 mL of the dispersion was placed on GCE (d= 3 mm) and allowed to dry naturally. All measured potentials were converted to the reversible hydrogen electrode (RHE) using the following equation:

$$E_{RHE} = E_{Ag/AgCl} + 0.197V + 0.059pH \quad (1)$$

In 1 M KOH solution, linear sweep voltammetry (LSV), cyclic voltammetry (CV), electrochemical impedance spectroscopy (EIS), and chronoamperometry (CA) experiments were performed. The empirical Tafel formula was used to simulate the Tafel slope:

$$\eta = a + b\log[I] \quad (2)$$

Where η, I, b, and a are the overpotential, observed current density, Tafel slope, and the intercept, respectively. An amplitude of 5 mV was measured using EIS. All potentials were referred to the

RHE without further qualification.

2.4.3 Biomedical wastewater remediation tests

2.4.3.1 Cell culture

The Caco-2 human colorectal adenocarcinoma cells with suitable transfection hosts commonly used in toxicology and cancer research were obtained from the Pasteur institute of Iran. All experiments were performed in cells' 3-4th passage number. High glucose medium culture (DMEM) was supplemented with pen-strep antibiotic (100 units/ml and 100 µg/ml, respectively) and 10% fetal bovine serum. Cells were kept in an incubator with 5% CO_2 and 98% humidity at 37°C.

2.4.3.2 MTT cell viability assay

The cytotoxicity effects of $NiTiO_3$/C (0.05-0.8 µg/mL) and F-doped $NiTiO_3$/C (0.05-0.8 µg/mL) were recognized under irradiation and dark via MTT viability assay. At first, Caco-2 cells were cultivated in a 96-well plate (6×10^3 cells/well) and incubated for 24 hours. Then, the cells were exposed to different concentrations of the photocatalysts. MTT assay was carried out after the overnight incubation. Briefly, 20 µl of MTT dye (5 mg/mL) was added to each well. After 4 hours of incubation at 37°C, the wells were depleted totally. In the next step, 200 µL of DMSO was added to each well and incubated for 20 min at room temperature in the dark. Finally, the absorbance of the wells was read at 570 nm with an Elisa reader.

2.4.3.3 ROS Evaluation through Dihydroethidium (DHE) Assay

Initially, Caco-2 cells were treated with IC50 concentration of $NiTiO_3$ (0.3 µg/mL) and F/$NiTiO_3$ (0.15 µg/mL). A ROS detection kit (DHE) assessed intracellular ROS production. The test was performed based on the kit's protocol as previously described [93]. The treated cells were rinsed with cold PBS after 24 h of incubation. For staining, DHE was used and incubated for 30 min at dark. Cytation5 cell imaging multi-mode reader was

used to evaluate ROS quantity amounts and prepare the microscopic images.

2.4.3.4 Caspase 3/7 activity detection

Cayman Caspase 3/7 ELISA assay kit was used to detect caspase 3/7 activity level. After seeding Caco-2 cells and treatment with IC50 concentration of $NiTiO_3$/C (0.3 µg/mL) and F-doped /$NiTiO_3$/C (0.15 µg/mL) for 24h, the assay was performed based on the kit instruction. Obtained results have been illustrated in column graphs for a better understanding.

2.4.3.5 Assessment of the mitochondrial membrane integrity

Caco-2 cells were treated with $NiTiO_3$/C (0.3 µg/mL) and F-doped /$NiTiO_3$/C(0.15 µg/mL) for 24h to evaluate the mitochondria membrane potential (MMP). In brief, after the incubation time, cells were washed with PBS. Then, JC-1 fluorescent dye was used for the cell staining. The final analysis was performed by Cytation5 cell imaging multi-mode reader in two different excitation/emission wavelengths (485/530 and 530/590). As the Red/Green fluorescent ratio indicates MMP changes, apoptosis activation significantly decreases in this ratio.

2.4.3.6 Apoptosis induction assessment

Flow cytometry apoptosis analysis assessed the apoptotic cells' number in Caco-2 treated cells with $NiTiO_3$/C and F-doped $NiTiO_3$/C. After seeding Caco-2 cells and treatment with $NiTiO_3$/C (0.3 µg/mL) and F-doped $NiTiO_3$/C(0.15 µg/mL) for 24h, cells were de-attached with EDTA buffer and washed with cold PBS twice. Then, about 10^6 cells were suspended in 500µL of PBS. In the next step, Annexin V-FITC (Sigma, A9210) and PI (Sigma, P2667) were utilized according to the kit instruction. Finally, apoptotic cells were evaluated by Flow cytometry while all the results were acquired in 10000 event count.

3. Results and discussion

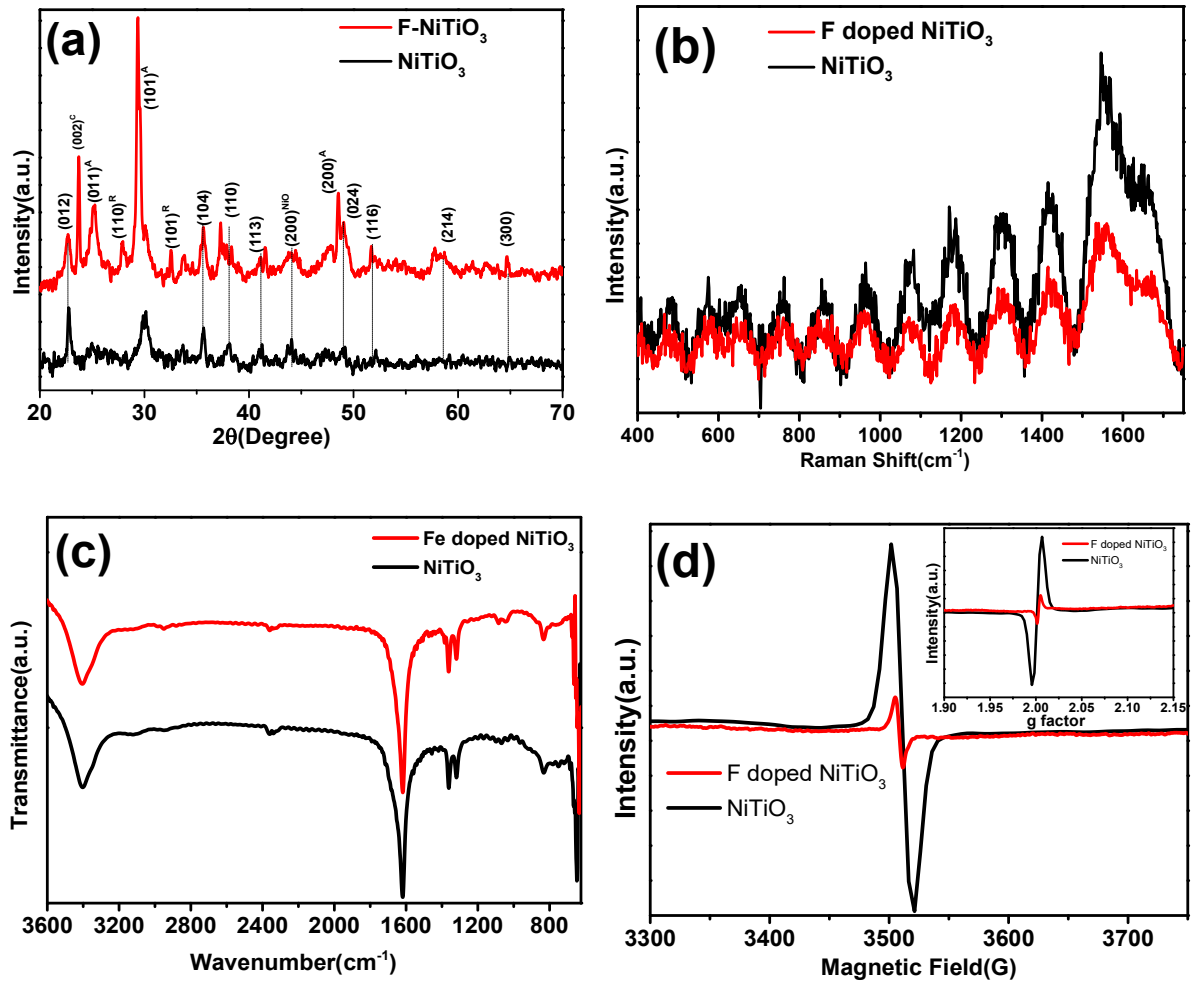
3.1 Structure, composition, and Morphology of the Photocatalysts

Fig. 1(a) shows the XRD patterns of $NiTiO_3$/C and F-doped $NiTiO_3$/C photocatalysts hydrothermally synthesized at 423 K. The characteristic XRD peaks at 24.1°, 33.1°, 35.6°, 40.8°, 49.5°, 53.9°, 62.5°, and 64° could be attributed to the (012), (104), (110), (113), (024), (116), (214) and (300) reflections for ilmenite $NiTiO_3$ (JCPDS no. 33-0960) [94]. In the XRD pattern of F-doped $NiTiO_3$/C, the peaks at 25.1°, 29.4°, and 48.5° are related to the anatase phase of TiO_2. In comparison, peaks at 27.7°, 32.8°, and 44.2° are characteristic peaks of rutile TiO_2 and NiO, respectively [95]. The diffraction peak around 26.5° is the typical peak of carbon [96]. However, the absence of peaks corresponding to F ions in the XRD pattern of the F-doped $NiTiO_3$/C is due to the low dopant concentration and the uniform distribution of ions in the prepared samples, which can not be detected by XRD. Fig. 2(b) presents the Raman spectra of the carbonized pristine $NiTiO_3$ and F-doped $NiTiO_3$ composites. Due to the high structural disorder degree at short range, no Raman active modes were observed below 400 cm^{-1}. It should be noted that crystal size, crystal structural order degree, and differences in synthesis method caused the changes in the Raman peaks position [97]. Raman active modes of $NiTiO_3$ and F-doped $NiTiO_3$ composites confirm the rhombohedral Structure with the positions of the peaks at 483(E_g), 654.2(E_g), 758.3(A_1g) cm^{-1} [98] where Raman modes at 654.2, 758.3 cm^{-1} are stretching vibrations of TiO_6 octahedral [99]. On the other hand, characteristic stretching peaks 430(Eg) and 570 (A1g) cm^{-1} are related to the rutile TiO_2 [100]. The peaks at 1077, 1180, 1300, and 1552 cm^{-1} belong to NiO as impurity and carbon content in synthesized composites, respectively[101].

Fourier Transform infrared (FT-IR) spectra of carbonized $NiTiO_3$ and F-doped $NiTiO_3$ nanocomposites in the range 400–4000 cm^{-1} have been demonstrated in Fig. 1(c). The absorption bands at 3408 and 1611 cm^{-1} are attributable to the v(O-H.) stretching and

bending vibrations, respectively, indicating the existence of adsorbed water molecules [102]. The peak at 2347 cm^{-1} corresponds to the existence of CO_2 residues from atmospheric contaminants. The strong bands below 800 cm^{-1} are attributed to stretching (Ti–O) and (Ni–O) bands. The peaks between 900 -1300 cm^{-1} can be assigned to ν(C-C), ν(C-O), and ν(C-O-C) bands [103]. Fig. 1(e) demonstrated the photophysical characteristic of bare $NiTiO_3$/C and F-doped $NiTiO_3$/C investigated using UV-Vis diffuse reflection spectroscopy (DRS). The inset of Fig.1(e) shows the plot of $(\alpha hv)^2$ versus the energy of the absorbed light. The absorption edges of $NiTiO_3$/C and F-doped $NiTiO_3$/C are about 405 nm ($E_g = 3.49$ eV) and 443 nm ($E_g = 3.00$ eV), respectively. Although the addition of F and carbon materials in the prepared photocatalyst does not lead to the significant bandgap shift toward higher wavelengths, however, since the O^{2-} radius is bigger than F^- ion (1.4 ˚A vs.1.33 ˚A), this size difference may affect the structural stability and lattice parameters of the compound. Therefore, F substituting O in the Ni-O bonds changes the local disorder and defects distribution and provides a high amount of vacancies in the structure, which can trap the photogenerated electrons and adsorb O_2 molecules and reduce into $^{\bullet}O_2^-$ [104]. The electron paramagnetic resonance spectroscopy (EPR) measurement has been performed to detect the paramagnetic species of bare $NiTiO_3$/C and F-doped $NiTiO_3$/C photocatalyst, as shown in Fig. 1d. Compared to $NiTiO_3$/C (g =2.001), the intensity of peak belongs to F-doped $NiTiO_3$/C composite (g=1.9954) has been increased. Since the F ions are highly electronegative, they can replace the oxygen in the photocatalyst surface and convert Ti^{4+} to Ti^{3+} states, which are considered as active sites for forming superoxide ions [105]. It was also confirmed that oxygen vacancies could form by F doping by removing either a bridging oxygen atom or an in-plane oxygen atom [106]. In order to examine electron transmission and recombination rates, photoluminescence (PL) analysis was conducted at room temperature with an excitation

wavelength of 320 nm (Fig 1f). The greater the PL intensity, the higher the recombination rate of photoexcited charge carriers in the photocatalyst. Low PL intensity, on the other hand, indicates a greater possibility of carrier recombination. According to the results, the F-doped $NiTiO_3$/C has a lower PL intensity than $NiTiO_3$/C, indicating a separation of charge carriers. As a consequence, incorporating F ions onto $NiTiO_3$/C nanocomposite could lessen electron-hole recombination[65].



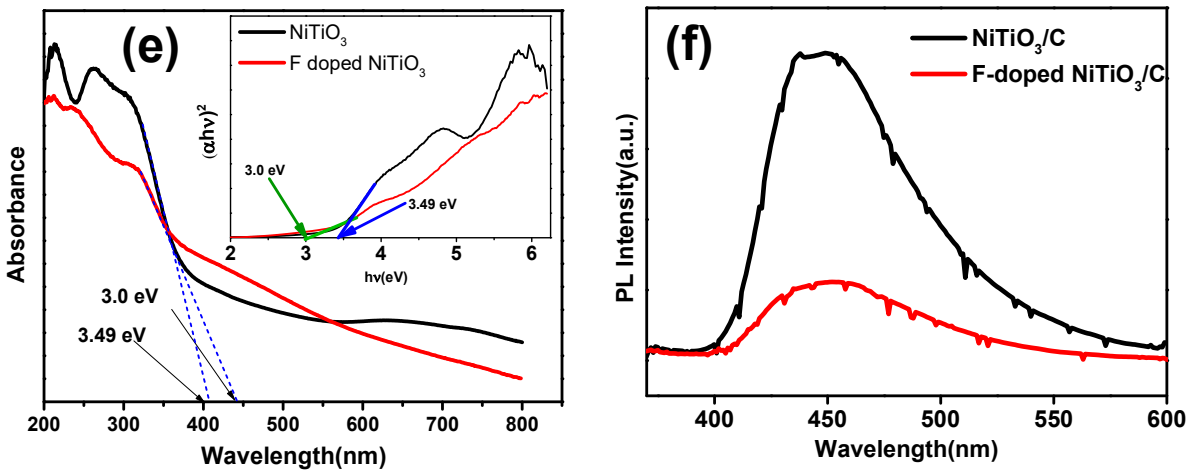


Fig. 1. (a) XRD patterns, (b) Raman Spectra, (c) FTIR Spectra, (d) UV-vis diffuse reflection spectroscopy results, (e) EPR spectroscopy, and (f) PL spectra of the structures.

XPS analysis provided information on the chemical state of the elements in the structure. The existence of Ni^{2+} can be testified in the high-resolution Ni 2p XPS spectrum (Fig. (2a)). The two typical peaks can be assigned to Ni $2p_{3/2}$ and Ni $2p_{1/2}$, which in the case of $NiTiO_3$/C presented at 854.6 and 872.3 eV, respectively. While for F-doped $NiTiO_3$/C, these peaks have been shifted to 856.1 and 874.6 eV, respectively (Fig. 3a). The other peaks at 860, 862.1, and 877.8 eV in the case of $NiTiO_3$/C and at 861.2 and 880.42 eV in the F-doped $NiTiO_3$/C case can be assigned to the satellite peaks [107]. In the Ti 2p spectra (Fig. 2b), peaks at binding energies of 462.3 eV and 456.6 eV are related to Ti $2p_{1/2}$ and Ti $2p_{3/2}$, respectively [108]. In the Ti 2p spectra of F-doped $NiTiO_3$/C, peaks belong to Ti $2p_{1/2}$ and Ti $2p_{3/2}$ located at 464.13 eV and 458.6 eV, respectively (Fig. 3b). As demonstrated in Figs 2c and 3c, the core-level spectra of the O 1s region have been deconvoluted into o three peaks. The peak at 528 eV can be due to O^{2-} or metal oxide such as Ti-O [16, 67]. The peak at 529 eV corresponds to Ni-O or C-O-Ni. Meanwhile, the signal at 531.80 eV is due to C-O species on the carbon surface [72]. Due to the F-doping location, the intensity of these peaks has been changed. Fig. 2d shows the deconvoluted spectra of C1s with a peak at 282.98 eV assigned to the C-C bond. Similarly, the weak signal at 284.1 eV is due to oxygen

functional groups as O-C or C-O-C. The peak at a binding energy of 282.8 could correspond to C=O or O-C=O functional groups [72, 109]. As shown in Fig. 3d, for F-doped $NiTiO_3$/C, just two peaks remain at 284.1 and 288.9 eV related to the C-C bond and O-C=O functional group, respectively. The F1s XPS spectrum in Fig. 3e demonstrated the characteristic peaks at 688.8, 685.2, and 683.5 eV correspond to the covalent and semi-ionic F species, respectively[110, 111].

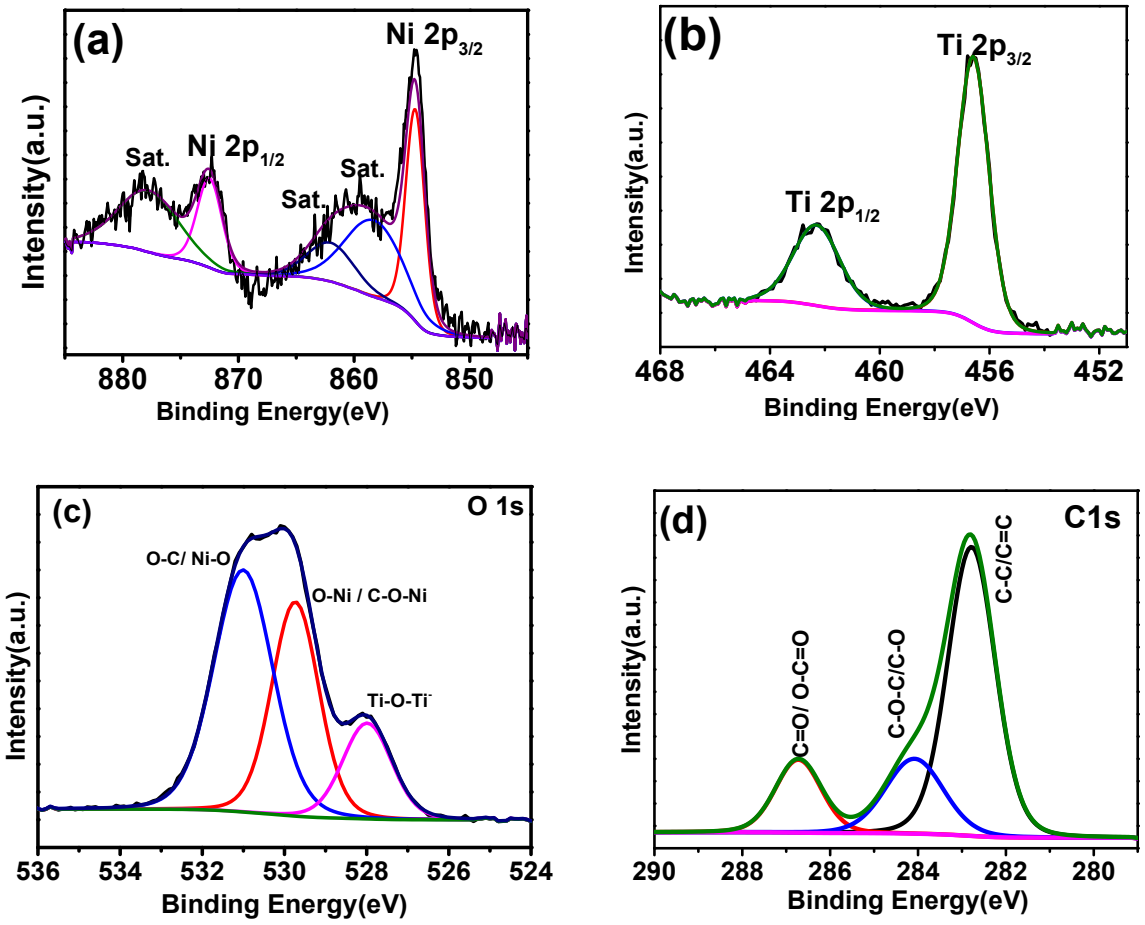


Fig. 2. XPS spectra of the $NiTiO_3$/C structure:(a) Ni 2p, (b) Ti 2p, (c) O 1s, (d) C 1s.

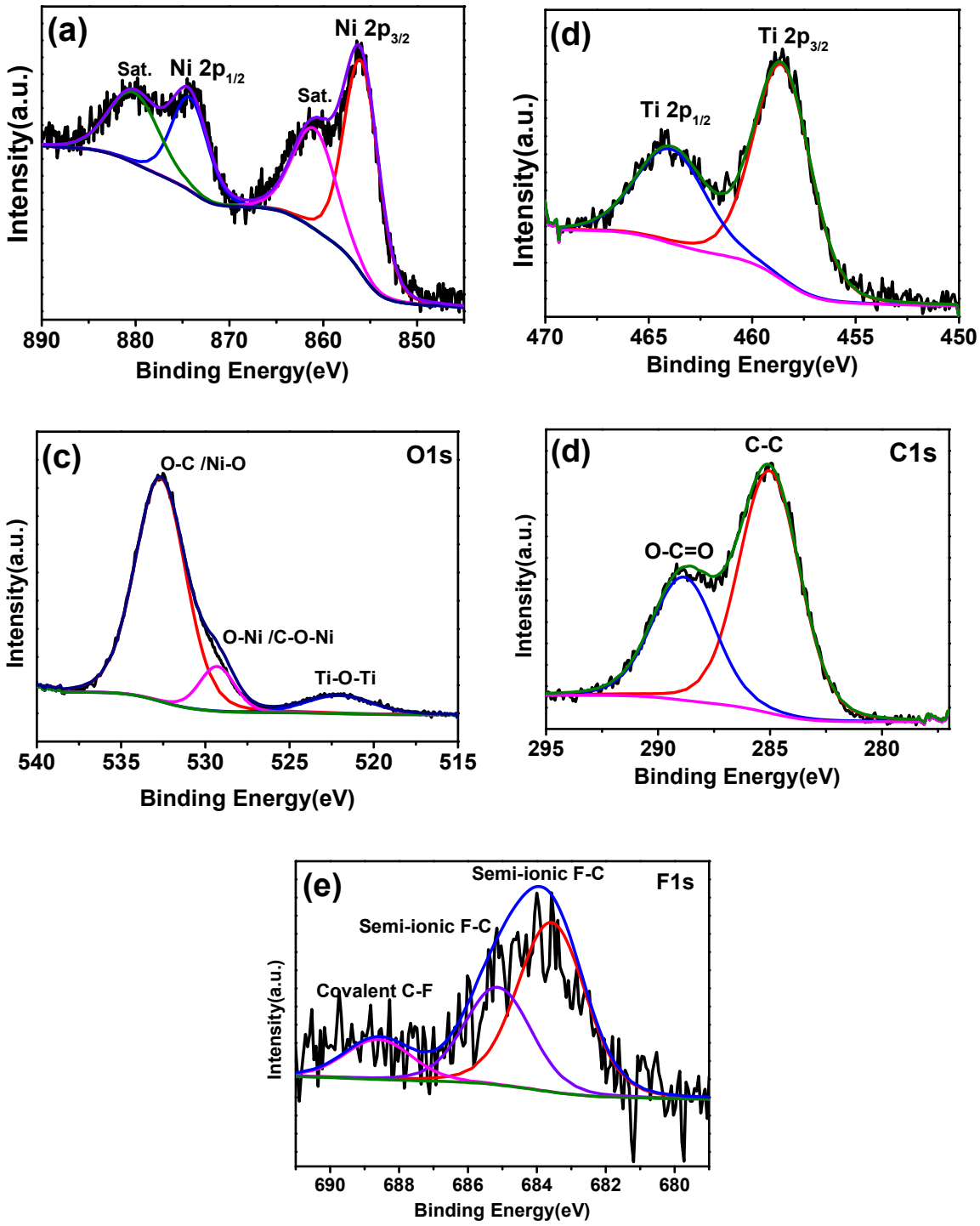


Fig. 3. XPS spectra of the F-doped $NiTiO_3$/C structure:(a) Ni 2p, (b) Ti 2p, (c) O 1s, (d) C 1s, (e) F 1s.

Fig. 4 shows the interfacial morphologies and surface composition of $NiTiO_3$/C characterized by FESEM, TEM, and elemental mapping analysis. As shown by the SEM

image in Fig. 4a, $NiTiO_3$/C comprises spherical nanoparticles and rod-like aggregates (2–3 μm in length and ~50 nm in diameter), which are demonstrated by the TEM images in Figs. 4e and 4f. These results indicate the clear and tight interface between $NiTiO_3$ and carbon coated on the surface of the rods. Elemental mapping analysis indicates the uniform distribution of nickel, titanium, and oxygen elements (Fig. 4b-d). As visualized by Fig. 5a, and b, the incorporation of F ions significantly influenced the $NiTiO_3$ and changed the morphology to an octahedral shape. Elemental mapping and EDS analysis confirmed the presence of F and uniform distribution of all elements.

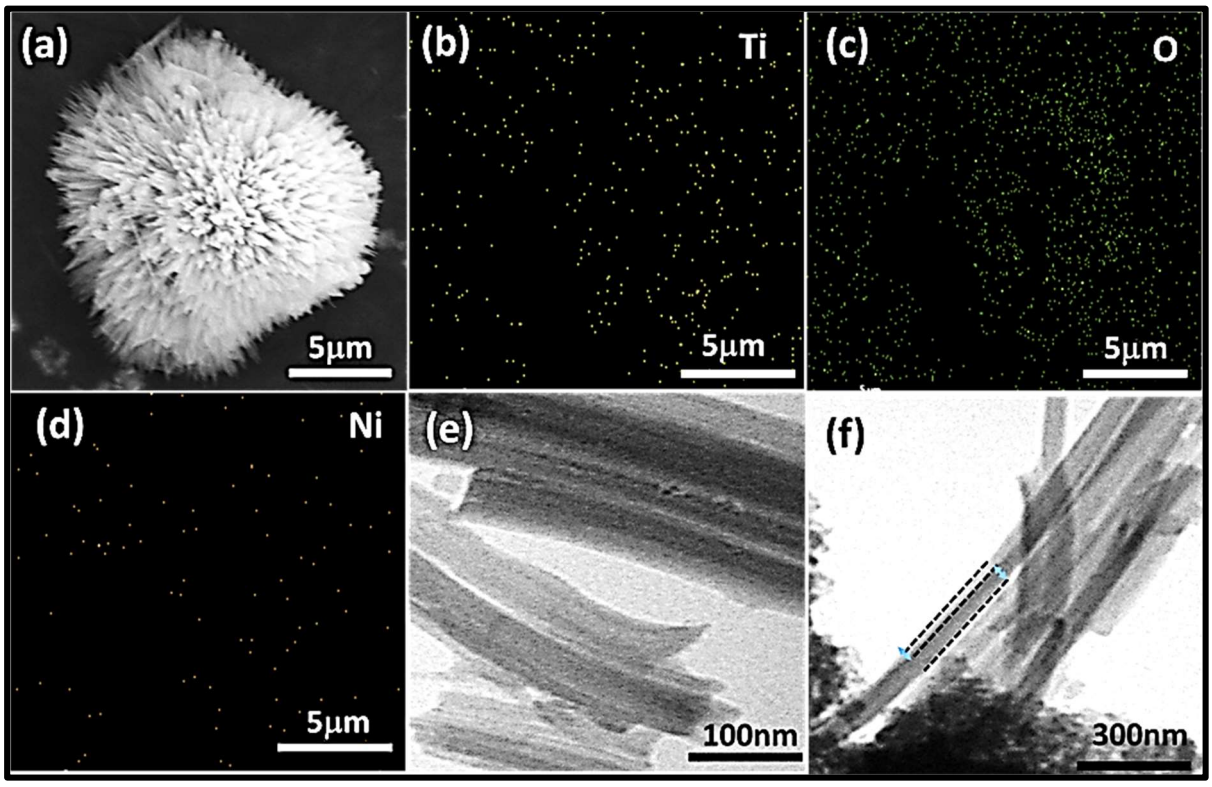
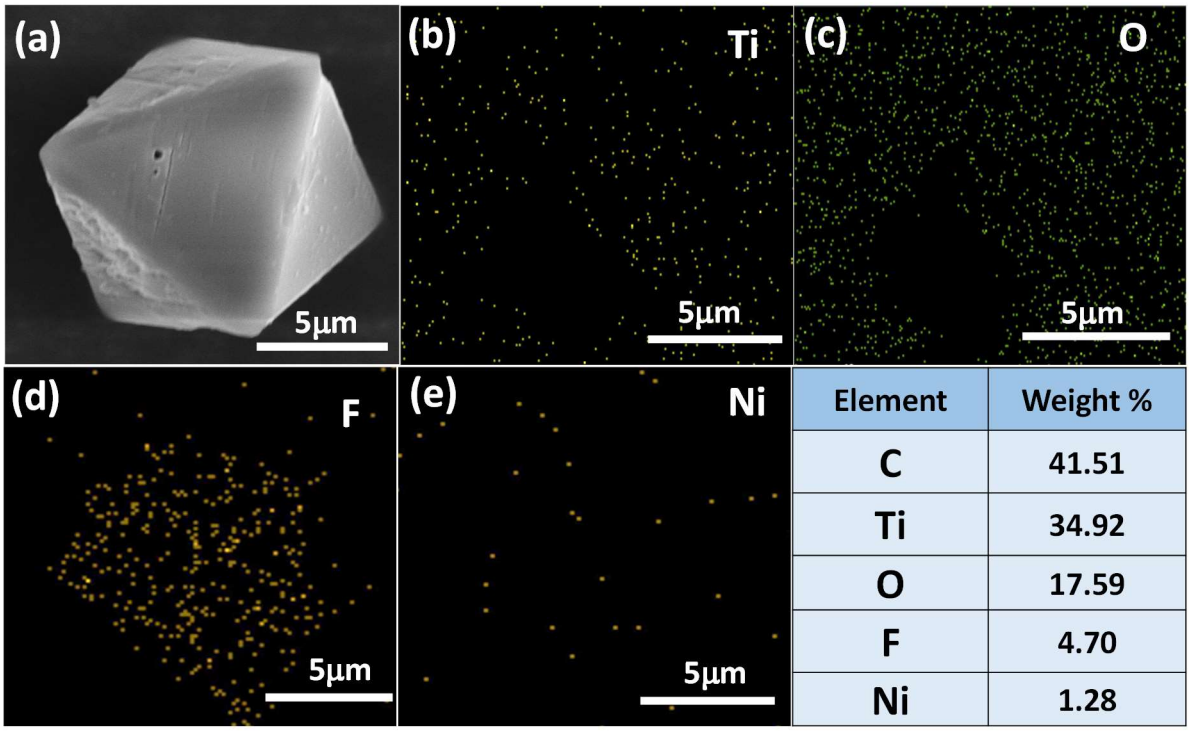


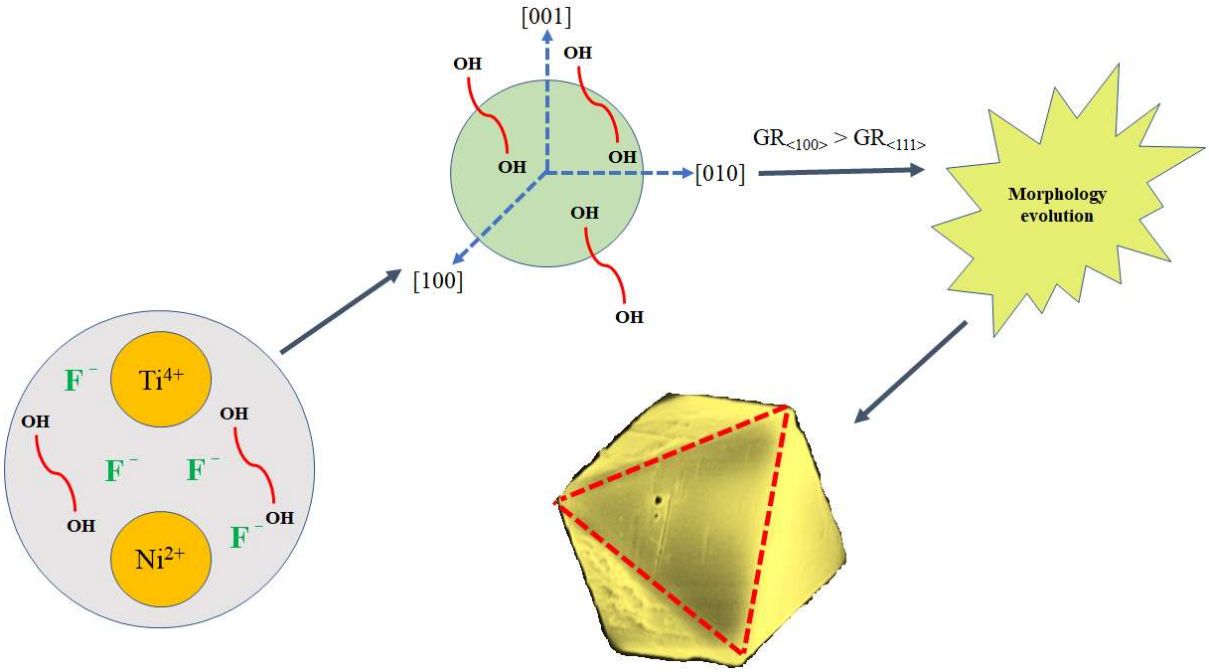
Fig. 4. (a) FESEM image, (b)-(d) elemental mapping analysis, and (e)-(f) TEM images of $NiTiO_3$/C.



Element	Weight %
C	41.51
Ti	34.92
O	17.59
F	4.70
Ni	1.28

Fig. 5. (a) FESEM image, (b)-(e) elemental mapping analysis, and EDS analysis of F-doped $NiTiO_3$/C.

According to the previous reports on the formation of octahedral-shaped crystals in the ethylene glycol (EG) medium and the presence of fluorine ions, the mechanism of crystal growth can be proposed as follows [2, 22]: the initial nuclei of F-doped nickel titanate crystals were formed through the reactions between the nickel and titanium ions, released from the metal-ethylene glycol complex, with the fluorine ions. The hydroxyl groups from EG play a key role in regulating the crystal growth direction and becoming the final crystal octahedral shape. Due to the increased growth rate (GR) along the <100> vs. <111> planes under the hydrothermal conditions, the morphology underwent an evolution from spherical for the initial nuclei to aciform and, ultimately, regular octahedral for the final product. The crystals then grew and became larger based on the Ostwald-ripening theory. The abovementioned process was schematically illustrated in Scheme 1.



Scheme 1. Schematic description of the growth pathway resulting in octahedral-shaped F-doped $NiTiO_3$/C crystals.

3.2 Photo-catalytic performance tests

3.2.1 CO_2 photo-catalytic reduction

The CO_2 photoreduction performance of prepared photocatalysts was conducted over the as-prepared photocatalysts in the presence of water vapor. The obtained results are exhibited in Fig.6 and Table 1. Fig.6a shows that the CO production rate was intensified with illumination time over the pristine $NiTiO_3$ as it reached higher than 100 µmol g- h^{-1}. The higher selectivity of pristine $NiTiO_3$ towards CO can be attributed to its inherent properties and surface chemistry leading to strong CO adsorption. In this regard, the strong CO adsorption could promote the formation of CO-related intermediates and favors the production of CO rather than CH_4. When F ions are introduced to $NiTiO_3$/C, it can alter the surface chemistry and electronic properties of the catalyst. F dopants can create additional active sites and modify the adsorption behavior of reactant molecules.

This can lead to enhanced selectivity for specific reactions. Considering this, the F-doped $NiTiO_3$ followed a different trend compared to pristine $NiTiO_3$, and the production rate of CO increased to ~33 μmol.g^{-1}.h^{-1} after 3 h of the reaction time and then decreased to ~21.1 μmol g^{-1}.h^{-1}. From Table1, the CH_4 evolution rate over F-doped/$NiTiO_3$/C, 2.6 μmol g^{-1}.h^{-1}, was 1.6 times higher than the estimated rate over the pristine $NiTiO_3$, 1.6 μmol g^{-1}.h^{-1}, under visible light, highlighting the enhanced photocatalytic activity of nickel titanate after incorporating fluorine impurity into the bulk structure. In other words, the presence of fluorine dopants can improve the adsorption of CO_2 on the catalyst surface. This promotes the activation of CO_2 and facilitates its conversion to CH_4. Furthermore, the CH_4/(CO+CH_4) ratio reached 11.0 and 1.6 % over the F-contained sample and pristine $NiTiO_3$, respectively, suggesting that F-doped $NiTiO_3$/C selectively converts CO_2 to methane while pristine $NiTiO_3$ acts more selective to reduce CO_2 to CO. In fact, F dopants weaken CO adsorption on the catalyst surface. Due to this, there is less likelihood of CO forming CH_4, resulting in lower CO selectivity. It has been revealed that multiple reaction steps of CO_2 reduction to CO need two photoinduced electrons and two protons. However, eight protons and eight electrons must be supplied to produce CH_4 through the reaction mentioned above [112]. Recycling tests were conducted to determine the structural stability of the prepared photocatalysts after subsequent use. As shown in Fig.6 b, the activity for methane production yield smoothly decreased after five times of repeated use for both F-doped $NiTiO_3$/C and $NiTiO_3$/C, indicating that the prepared photocatalysts profit from a stable texture for being used in practical applications. According to the reports [46, 113], the carbon-coating strategy plays a vital role in ameliorating the chemical stability and structural solidarity of the catalytic materials under irradiation. Benefiting from the ethylene glycol medium synthesis, $NiTiO_3$, and F-doped $NiTiO_3$ structures were efficiently carbon-coated, as shown by the XPS and TEM

results, leading to their enhanced photo-catalytic stability after multiple times of using for NOx removal.

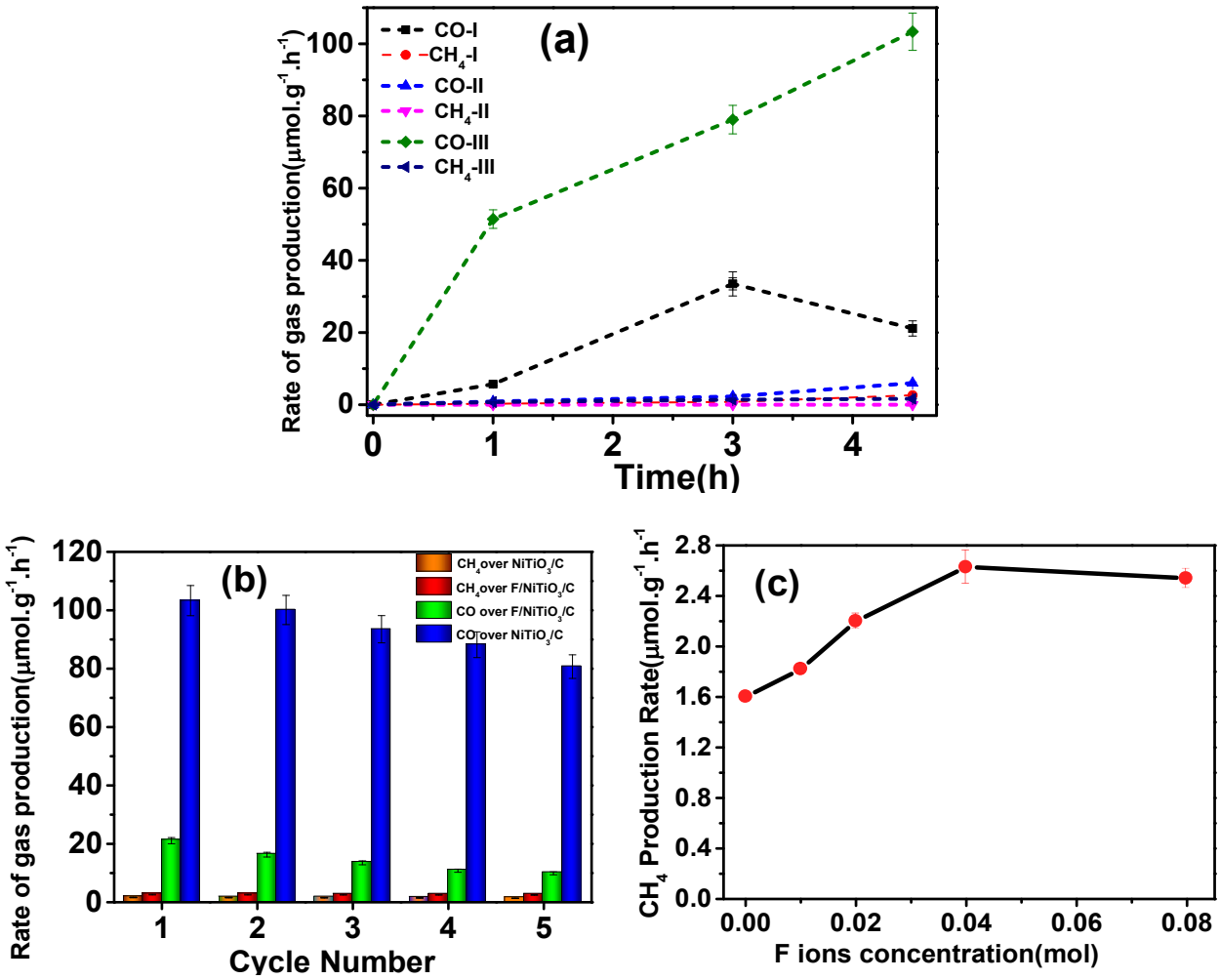


Fig. 6. (a) The results of CO_2 photoreduction experiments over F-doped $NiTiO_3$ (I), TiO_2-P25 (II), and pristine $NiTiO_3$ (III), (b) Stability experiments of as prepared photocatalysts after five cycles, and (c) The effect of F doping on CO_2 catalytic reduction over F-doped $NiTiO_3$ photocatalyst.

Table 1. The CO photoreduction over the different photocatalysts

Yield in μmol. g^{-1}[cat]. h^{-1} over:						$CH_4/(CH_4+CO)$ (%)		
$F/NiTiO_3$		P25		$NiTiO_3$		$F/NiTiO_3$	P25	$NiTiO_3$
CO	CH_4	CO	CH_4	CO	CH_4			

0	0	0	0	0	0	0	0	0
5.7	0.3	0.9	0	51.4	0.7	4.7	0	1.4
33.5	0.8	2.3	0	79.0	1.4	2.3	0	1.7
21.1	2.6	6.0	0	103.4	1.6	11.0	0	1.6

Fluorinated homogeneous (such as ionic liquids and small organic molecules) and heterogeneous systems (e.g., polymers, porous organic networks, covalent triazine frameworks, carbon materials, metal-organic frameworks, metal oxides, and membranes) have been paid much attention to CO_2 capture and fixation within broad and practical applications [114]. Even though some of the above systems possess inherent merit for the aforementioned purposes, the highly serendipitous contribution of fluorine defects and their essential role has always been highlighted. The presence of fluorine impurities influences the uptake capacity and sorption kinetics through various physicochemical interactions with the metal and non-metal moieties, resulting in enhanced CO_2 capture over the supports mentioned above. Also, the previous research demonstrated that F-doped materials have higher catalytic selectivity in the CO_2 reduction reactions compared with the non-fluorous counterparts, which is attributed to the promoted activation of substrates on the surface, tuning the electronic properties and unique electrochemical interactions considering fluorine chemistry [115].

The F doping strategy is frequently indicated to be effective in enhancing the CO_2 reduction rate and efficiency under electrocatalytic conditions [116]. From a mechanistic point of view, fluorine kinetically boosts the electroactive surface area and amends the charge transfer process, facilitating the CO reduction reaction steps. About the fluorinated photo-catalytic systems, the mechanism of action sounds pretty different due to the involvement of incident photons. Firstly, fluorine centers on the surface improve the CO_2 uptake performance and its activation under humid conditions for the efficient trigger of the photoreduction pathway [117].

The fluorine existence can also regulate the electronic properties of inherent catalytic active sites over the bulk structure, resulting in the formation of desired products, methane, in terms of energy crisis. According to earlier research, F impurities act as electron-withdrawing centers and effectively extract the photogenerated electrons from the photo-catalytic medium [118], resulting in proper charge carrier separation and higher photocatalytic efficiency. However, our findings show that CO_2 photo-catalytic reduction over the as-prepared materials was intensely affected by the F content (Fig.6c). The obtained results depicted that the CH_4 production rate firstly increased with the increase of F content in the synthesis medium up to 0.04 mol and then decreased, implying that there is an optimal concentration of F doping in the $NiTiO_3$ structures towards reaching the best performance to reduce CO_2, which is in agreement with previous studies regarding semiconducting materials. The reason could be attributed to a balance between the amendment of morphological properties and the creation of sufficient active sites resulting from F doping and electronic characteristics leading to sufficient charge carriers separation.

3.2.2 Electrocatalytic water splitting

To evaluate the electrocatalytic water splitting performance, the oxygen evolution reaction (OER) activity of pristine $NiTiO_3$ and F-doped $NiTiO_3$ structures was investigated by LSV with a typical three-electrode system, and obtained results were compared with the electrocatalytic activity of Pt/C catalyst. The LSV curves for OER at a scan rate of 5 mV s^{-1} in a 1 M KOH solution are shown in Figs. 7a, b, and c. Before depositing the catalysts materials on the GC electrode, its electrocatalytic behavior was determined by LSV for OER. As shown in Figs. 7a, b, and c, the current density of the GC electrode did not exhibit an evident rise in the potential range of 1.23 to 1.8 V. The LSV of all catalysts was recorded after the the10th and 1000th cycles of CVs. As shown in Fig. 7 a, the polarization curve of

the Pt/C catalyst drops dramatically after 1000 cycles of CV measurement, whereas the LSV curve of $NiTiO_3$/C and F-doped $NiTiO_3$/C remains similar to the 10th cycle (Fig. 7b and c). The findings clearly demonstrated that $NiTiO_3$/C and F-doped $NiTiO_3$/C have excellent catalytic activity and stability for OER through water splitting.

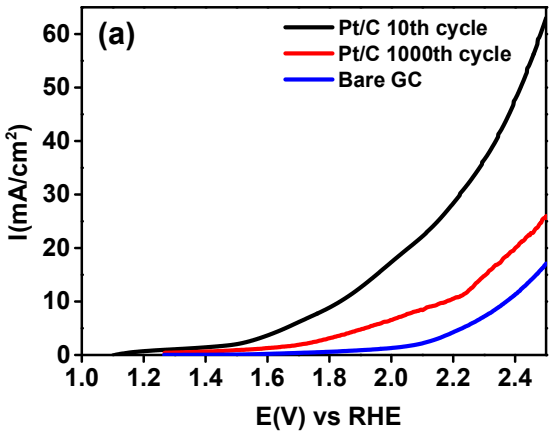
The comparison of LSV curves for bare GC, Pt/C, $NiTiO_3$/C, and F-doped $NiTiO_3$/C catalysts has been shown in Fig. 7d. A higher current was observed for the $NiTiO_3$/C and F-doped $NiTiO_3$/C electrodes compared to the Pt/C electrode, indicating improved catalytic performance toward OER. It would be instructive to compare the overpotential (η) for achieving a current density of 10 mA cm^{-2} as a metric standard relevant to solar fuel synthesis [119]. Based on the standard potential for the electrolysis of water to the oxygen of 1.23 V, the values were calculated to be 0.57, 0.68, and 0.27 V for Pt/C, $NiTiO_3$/C, and F-doped $NiTiO_3$/C, respectively.

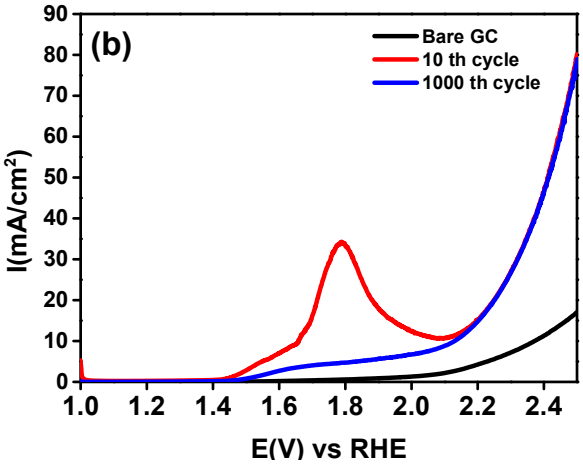
Typically, the Tafel slope is utilized to assess the OER kinetics, which can be calculated using Eq (2). In Fig. 7e, F-doped $NiTiO_3$/C demonstrates a smaller Tafel slope (81.2 $mVdec^{-1}$) than $NiTiO_3$/C (112.4 mV dec^{-1}) and Pt/C (124.4 mV dec^{-1}), indicating that F-doped $NiTiO_3$/C possesses favorable OER kinetics which could be due to the strong interaction between F and $NiTiO_3$/C.

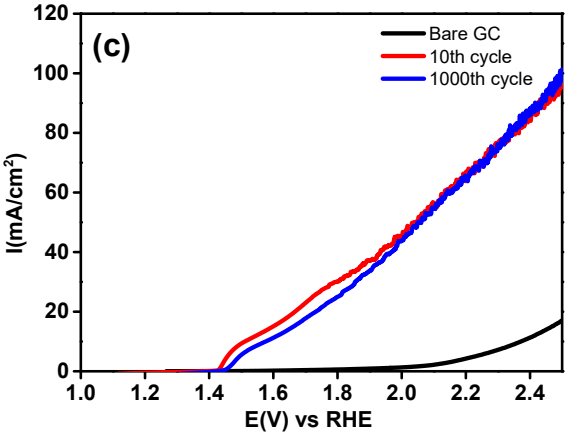
Charge transfer and ion diffusion kinetics of electrode materials have been studied using EIS analysis as a crucial and effective method [120, 121]. In order to further emphasize the advantages of the F-doped $NiTiO_3$/C catalyst for OER application, EIS measurements of Pt/C, $NiTiO_3$/C, and F-doped $NiTiO_3$/C were carried out at 1.6 V vs. RHE in 1 M KOH solution. The typical Nyquist plots and the corresponding circuit are shown in Figs. 7f and g. In the equivalent circuit (Fig.7 g), *Rs* represents the electrolyte resistance, *Rct* is the charge-transfer resistance, and CPE is the constant-phase element. The *Rct* values of Pt/C, $NiTiO_3$/C, and F-doped $NiTiO_3$/C were calculated to be approximately 120, 80, and 39 Ω,

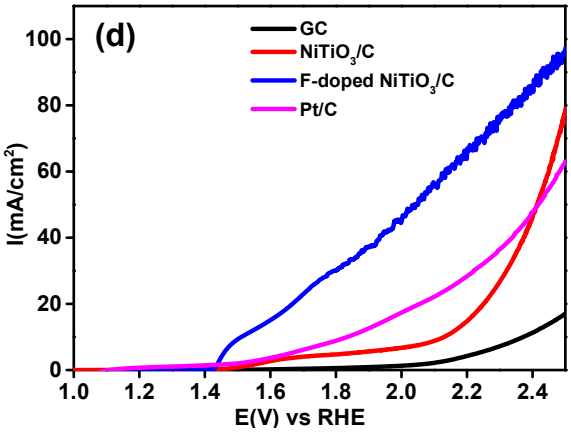
respectively, from the diameter of the semicircle, indicating that F-doped $NiTiO_3$/C has the lowest charge transfer resistance and the fastest kinetics in OER.

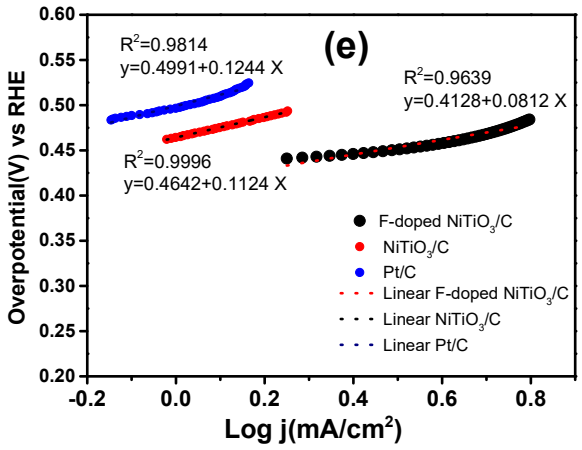
In order to assess the chemical stability and OER efficiency of fabricated electrodes under industrial operating conditions for alkaline electrolyzers, The performance of Pt/C, $NiTiO_3$/C, and F-doped $NiTiO_3$/C electrodes has been examined in 6 M KOH in a three-electrode compartment system for 18 hours at room temperature and pressure. While the F-doped $NiTiO_3$/C electrode demonstrated the best performance, with the current density starting at around 50 mA/cm^2 and stabilizing after about two hours, the pristine $NiTiO_3$/C also represented high stability. This observation can be obviously corresponded to the effect of the carbon-coating process on the electrocatalytic stability, making both photocatalysts promising candidates for real-world applications. Furthermore, F-doping enhances catalytic performance by providing a rich number of active sites on the octahedral faces and facilitating charge transfer. As shown in Fig. 7h, the stable current densities of 28, 18, and 12 mA/cm^2 at the voltage of 1.6 V were recorded for F-doped $NiTiO_3$/C, $NiTiO_3$/C, and Pt/C electrodes, respectively. According to these results, F-doped $NiTiO_3$/C exhibits the best electrocatalytic performance in chronoamperometry toward OER. This is most likely due to the synergetic effect of fluorine and $NiTiO_3$ constituents occurring through the F-metal bonding in a carboneous bulk, a justification in agreement with the results of CO_2 photo-catalytic reduction reaction.

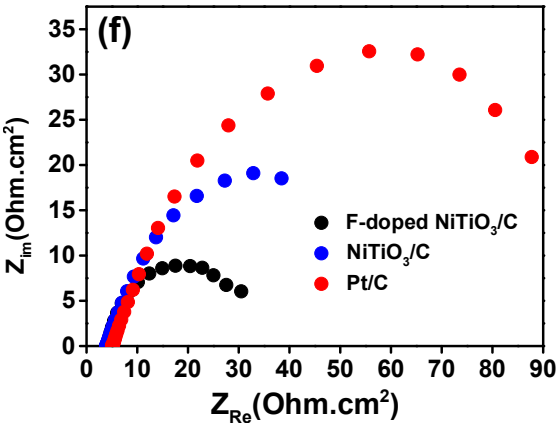

(a)
Pt/C 10th cycle
Pt/C 1000th cycle
Bare GC
I(mA/cm²)
E(V) vs RHE


(b)
Bare GC
10 th cycle
1000 th cycle
I(mA/cm²)
E(V) vs RHE


(c)
Bare GC
10th cycle
1000th cycle
I(mA/cm²)
E(V) vs RHE


(d)
GC
NiTiO3/C
F-doped NiTiO3/C
Pt/C
I(mA/cm²)
E(V) vs RHE


(e)
R²=0.9814
y=0.4991+0.1244 X
R²=0.9639
y=0.4128+0.0812 X
R²=0.9996
y=0.4642+0.1124 X
F-doped NiTiO3/C
NiTiO3/C
Pt/C
Linear F-doped NiTiO3/C
Linear NiTiO3/C
Linear Pt/C
Overpotential(V) vs RHE
Log j(mA/cm²)


(f)
F-doped NiTiO3/C
NiTiO3/C
Pt/C
Zim(Ohm.cm²)
ZRe(Ohm.cm²)

(g)

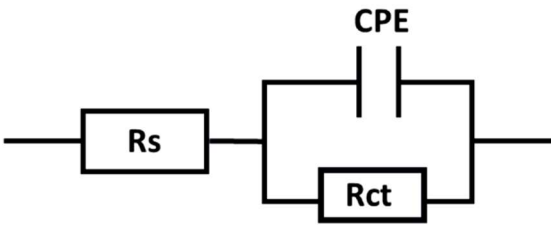


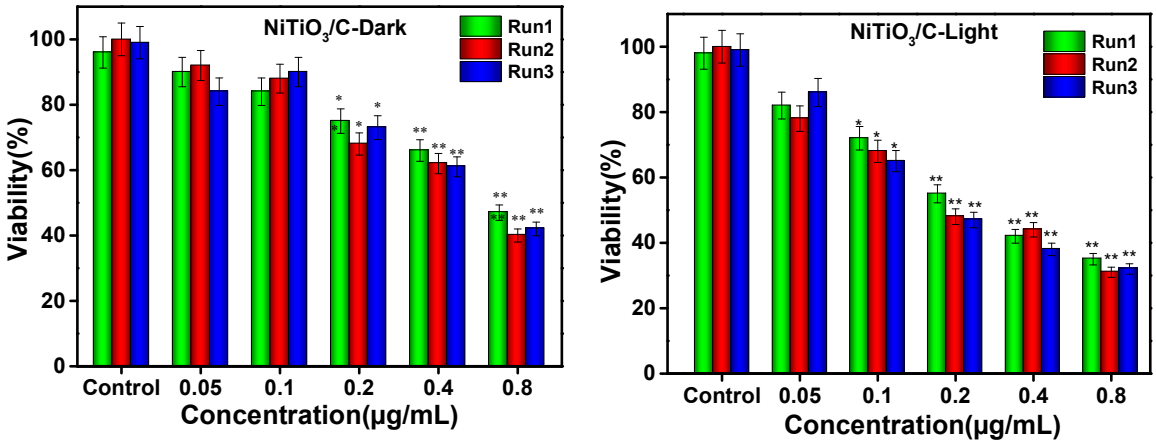
Fig. 7. The OER polarization curves in 1 M KOH with a scan rate of 5 mV s^{-1} after 10th and 1000th cycles for (a) Pt/C, (b) $NiTiO_3$/C, (c) F-doped $NiTiO_3$/C and (d) comparison of all electrodes with bare glassy carbon electrode (GCE). (e) Tafel plots for Pt/C, $NiTiO_3$/C, and F-doped $NiTiO_3$/C (f) Nyquist plots of EIS of Pt/C, $NiTiO_3$/C, and F-doped $NiTiO_3$/C from 100 kHz to 100 mHz with an amplitude of 5 mV and (g) the corresponding Nyquist plots. (h) the chronoamperometry curve for Pt/C, $NiTiO_3$/C , and F-doped $NiTiO_3$/C in 6 M KOH for 18 h.

3.2.3 Biomedical wastewater disinfection

3.2.3.1 Anti-proliferative effect of photocatalysts on Caco-2 cancer cells samples

MTT cell viability assay was performed to assess the cytotoxicity effects of $NiTiO_3$/C and F-doped $NiTiO_3$/C photocatalyst compounds. After 24 h of seeding Caco-2 cells in 96 wells plate, cells were treated overnight with different concentrations (0.05-0.8 μg/mL) of both $NiTiO_3$/C and F-doped $NiTiO_3$/C photocatalyst. It was found that under both irradiation and dark conditions, both photocatalysts exhibited cytotoxicity; however, the cytotoxicity was more potent under an irradiated condition. In addition, the results indicated that F-doped $NiTiO_3$/C has significantly higher anti-proliferative effects than $NiTiO_3$/C (Fig.8), which can also be justified based on the IC50 amount of $NiTiO_3$ and F/$NiTiO_3$ at dark (0.6 and 0.3, respectively) and under irradiation (0.3 and 0.15, respectively). Furthermore, the cytotoxicity effects of Ni nanoparticles have been confirmed on SKOV3 ovarian cancer

cells through the MTT cell viability assay [122]. Another research on the cytotoxic effects of Ni NPs on U87 cells revealed the inhibitory concentration as IC50 via MTT assay [123]. The recent study also evaluated the cytotoxicity of NiO nanoparticles (NPs) on various cancer cell lines such as MCF-7, Hep-G2, and HT-29 with MTT assay [124]. Their findings demonstrated the cytotoxic effect of Ni NPs in a dose-dependent manner. The same results were obtained in another research, which assessed Nickle Ferrite nanoparticles' cytotoxicity effect on MCF-7 and Hep-G2 cancer cells [125]. Moreover, A549 lung cancer cells treated by NiO NPs showed significant cytotoxicity to untreated control cells in response to increased concentrations [126]. Therefore, the findings of the current research were consistent with other similar studies in which the cytotoxicity of Ni NPs was evaluated on cancer cells. Further biochemical assays were carried out to investigate the possible working mechanism of cell death.



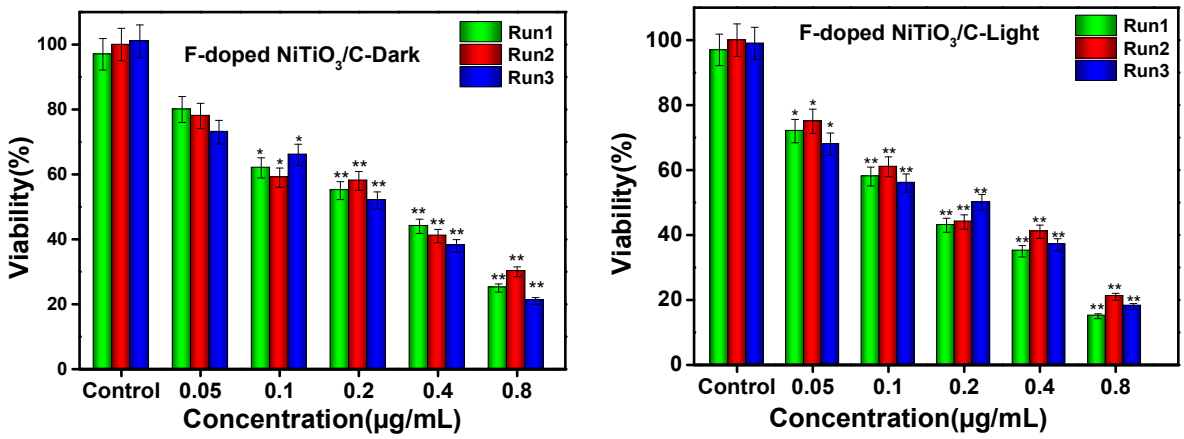


Fig. 8. Cytotoxic effects of $NiTiO_3$ and F/$NiTiO_3$ photocatalysts on Caco-2 cancer cells. All the results are mentioned as mean ±SD, * $P<0.01$, and ** $P<0.001$ are significant. Each point represents 3 repeats, each triplicate.

3.2.3.2 Assessment of ROS Generation by Photocatalysts

To evaluate the reactive oxygen species (ROS) level, a DHE stain assay was conducted. The microscopic images in Fig. 9a illustrate no considerable intensity of green emission in control cells, while the photocatalysts-treated cells have a striking fluorescent. As indicated in Fig. 9b and c, the F-doped $NiTiO_3$/C caused cells to produce significantly more intracellular ROS than $NiTiO_3$/C. A study on the effects of nickel-contained NPs against HT-29 colorectal cells showed that the increased cytotoxicity levels were related to the high amount of oxidative stress due to ROS production [124]. In another study, the effect of NiO NPs on A549 cells also proved the findings [127]. In addition, Ni NPs were tested on gastric cancer cells and reported to exhibit anti-proliferative effects and induce apoptosis through ROS production [128]. Here, apoptosis of mitochondria is confirmed by measuring the mitochondrial membrane potential and caspase activity.

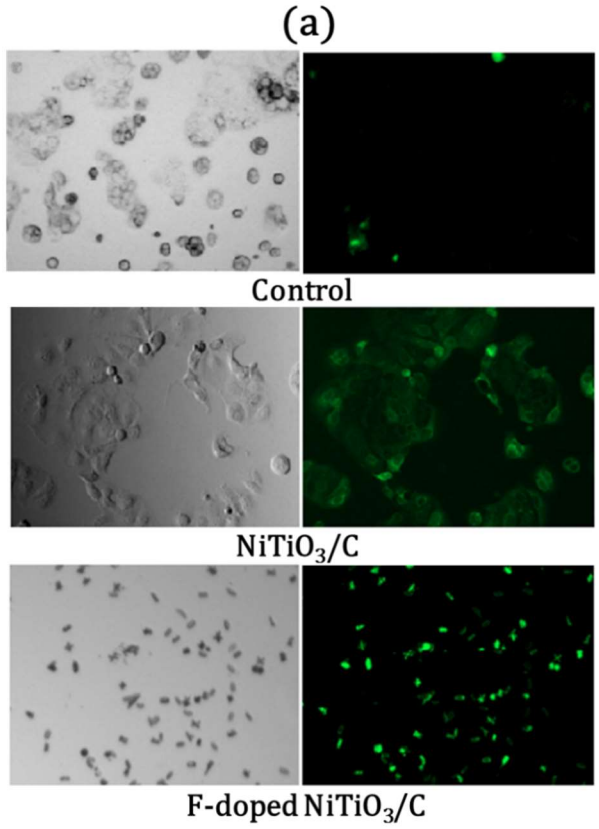


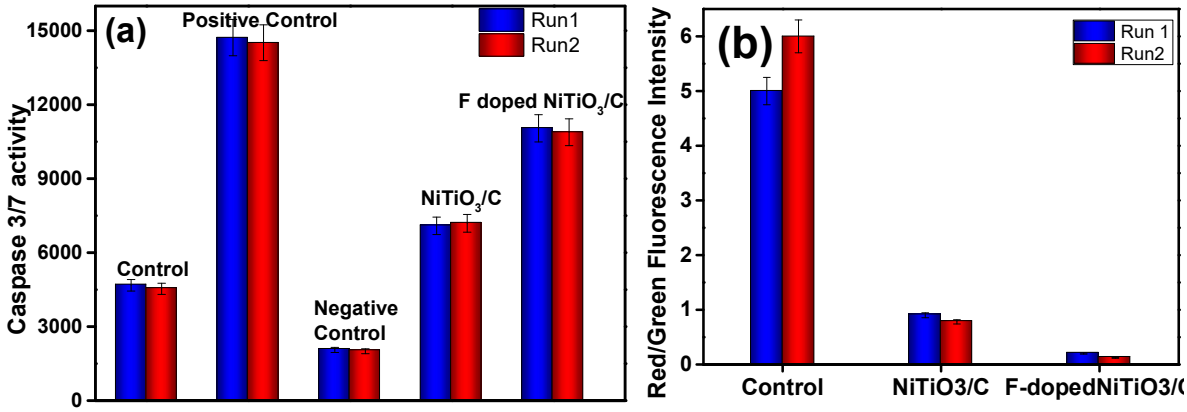
Fig. 9. (a) The microscopy images and the statistical column graphs of Caco-2 cells, DHE stained for ROS assay with IC50 concentration of (b) $NiTiO_3$/C (0.3 µg/mL), and (c) F-doped $NiTiO_3$/C (0.15 µg/mL).

3.2.3.3 Apoptosis cell death mediated by Caspases activation

A specific class of serine proteases, so-called "Caspases," play an essential role in apoptosis, from induction to DNA fragmentation. As Caspase activation is associated with apoptosis launching, the evaluation of the behavior of this enzyme can be beneficial in apoptosis studies [129]. According to obtained results in the current study, significant activation of caspases was detected in Caco-2 cells that were treated with $NiTiO_3$/C and F-doped $NiTiO_3$/C to control. Moreover, a significantly higher caspase activation rate was also observed in cells treated with F-doped $NiTiO_3$/C (Fig 10(a)). A previous study using Ni NPs to treat Hela cells revealed meaningful caspases 3 and 9 activations compared with the untreated control cells. They also claimed that Ni NPs could be a new approach

to cervical cancer treatment [130]. Here, the ability of $NiTiO_3$/C and F-doped $NiTiO_3$/C on caspases activation and apoptosis induction was demonstrated, and the status of mitochondria to assess the mechanism was evaluated.

Loss of mitochondria membrane potential was also measured in Caco-2 treated cells with $NiTiO_3$/C and F-doped $NiTiO_3$/C photocatalysts. As shown in Fig. 10b, both materials decreased the Red/Green fluorescence ratio, indicating a notable MMP decline. Moreover, the efficacy of F-doped $NiTiO_3$/C in mitochondria dysfunction was considerably more than $NiTiO_3$/C. The microscopic images clearly illustrate the abundance of red cells with intact mitochondria in control cells (Fig. 10c). Previous research conducted on HepG2 and MCF-7 cancer cells demonstrated the compound cytotoxicity effect after exposure to nickel ferrite NPs, which resulted in ROS formation and loss of MMP [125]. The results of the mentioned study were consistent with obtained data in the current research.



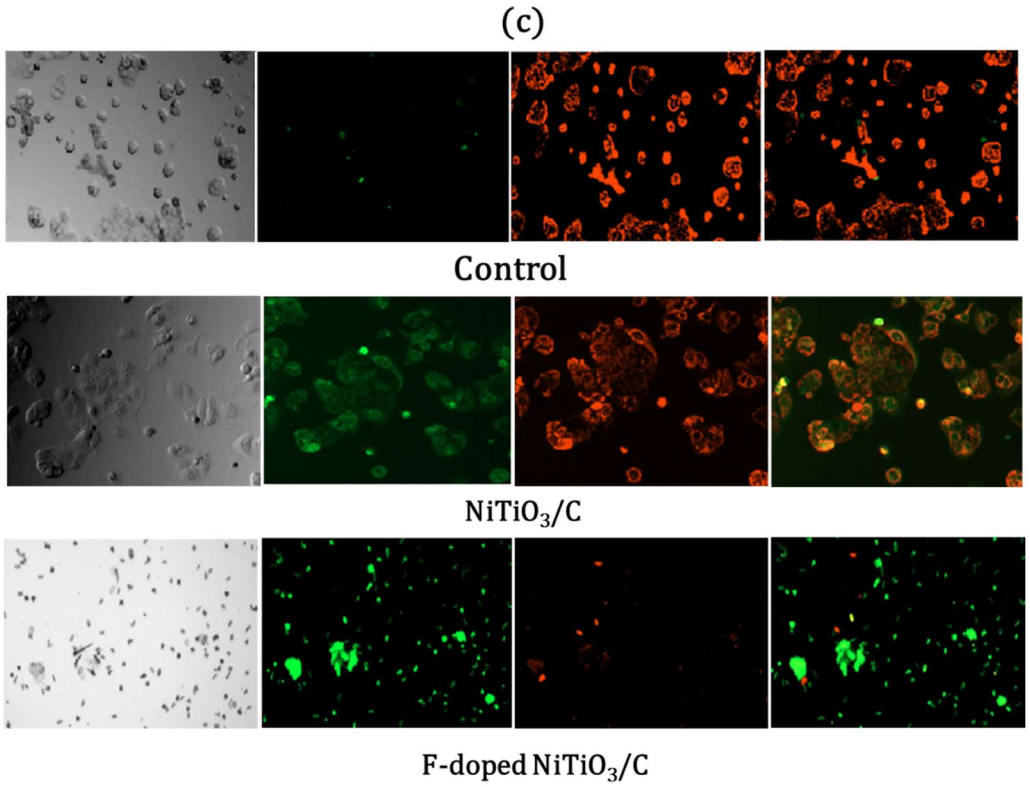


Fig. 10. (a) Caspase assay results on Caco-2 cells treated by the photocatalysts, (b) the quantitative results of mitochondria membrane potential changes, and (c) the fluorescent microscopic images of MMP assay on Caco-2 cells.

The final step of this study was to investigate the effects of photocatalysis on apoptosis cell death in different stages. Apoptosis assay results measured by flow cytometry were presented as dot-plot results in Figs. 11(a) to (c), and the column graph in Fig. 11(d). According to this assay, the percentage of the live cells, as well as the apoptotic cells (early+late), were detected in photocatalysts-treated cells and untreated control cells. As shown in Fig. 11d column graphs, apoptotic cells were significantly increased in response to $NiTiO_3$/C and F-doped $NiTiO_3$/C compared to the control. In contrast, F-doped $NiTiO_3$/C affected apoptosis induction more than $NiTiO_3$. An in vivo study was conducted to evaluate the effect of the nickel chloride compound on kidney tissue. The results demonstrated striking apoptotic cells and caspase activation in untreated control tissue [131]. Based on the current research findings, $NiTiO_3$/C and F-doped $NiTiO_3$/C

photocatalysts also induced the apoptosis cell death pathway, mediated by ROS formation and mitochondria dysregulation in Caco-2 cells. Considering all the discussions mentioned above from an in-depth literature review on nickel-based materials towards cancer cell inactivation, to our best knowledge, no work has been reported on exploring $NiTiO_3$/C and F-doped $NiTiO_3$/C yet, which highlights the novelty of present work compared to the previous research.

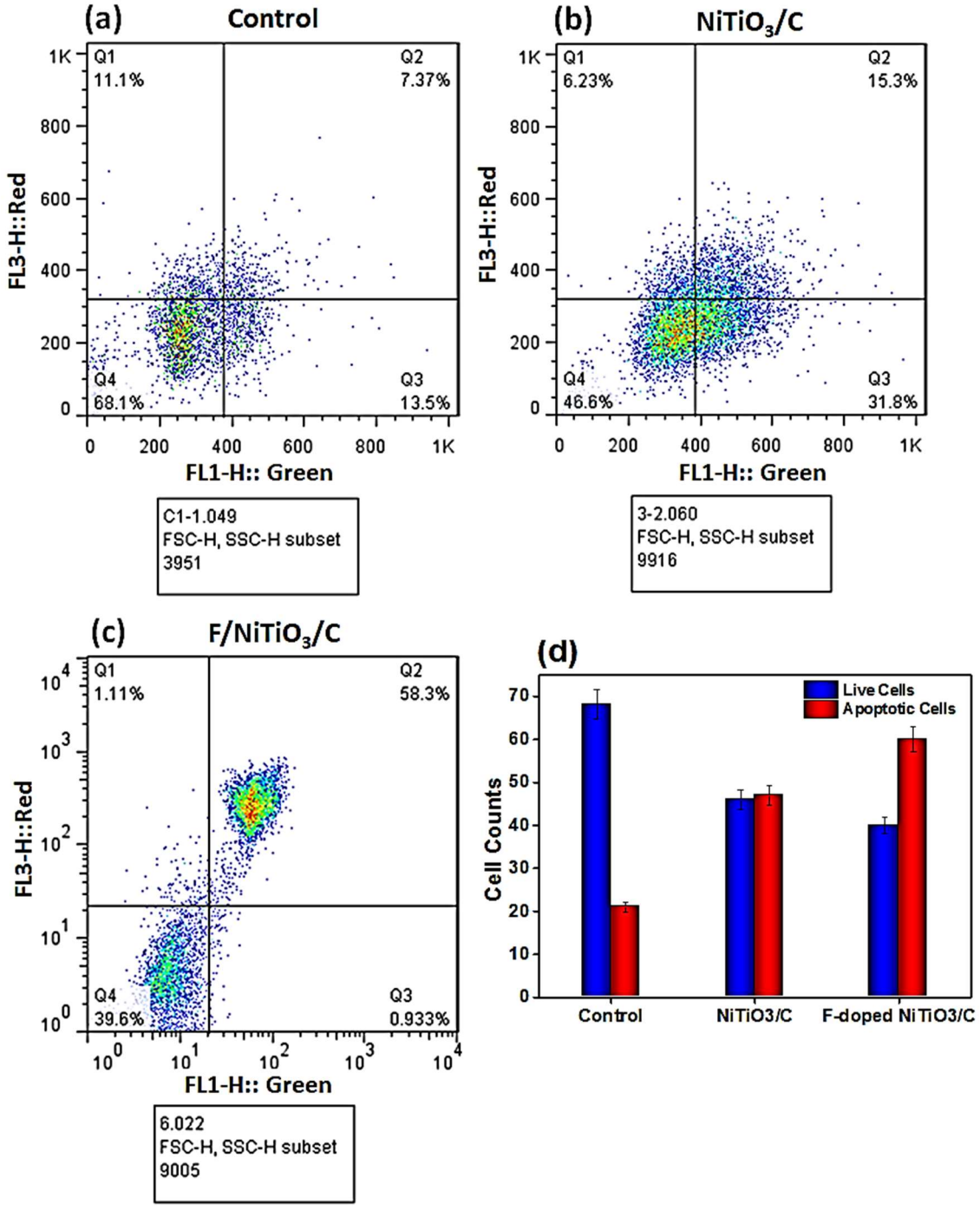


Fig. 11. Apoptosis assay results via flow cytometry: (a) to (c) dot-plot results and(d) column graph

4. Conclusions

Carbonized $NiTiO_3$ ($NiTiO_3$/C) and octahedral-shaped F-dopped $NiTiO_3$ (F-doped $NiTiO_3$/C) photocatalysts were successfully synthesized using a template-free hydrothermal method. The crystalline phases and morphological-chemical properties of synthesized photocatalysts were comprehensively identified through various analytical techniques, including XRD, XPS, SEM, EDX-elemental mapping, TEM, FTIR, PL, EPR, and Raman spectroscopy. The F-doping strategy alters the electronic characteristics of $NiTiO_3$/C. These changes can include alterations in the band structure (as confirmed by DRS results), energy levels, and electron mobility. As a result, the material's ability to absorb light and generate electron-hole pairs, which are essential for photo-catalytic processes, can be enhanced. In the presence of water vapor, the methane photocatalytic production rate of F-doped $NiTiO_3$/C was determined to be 1.6 times higher than that of pristine $NiTiO_3$/C. Furthermore, the catalytic activity remained almost constant even after five repeated uses. The amount of F dopant significantly influenced the CO_2 photoreduction rate, where the highest activity was observed with a content of 0.04 moles of NaF. Based on the electrocatalytic water splitting tests, the Rct value of F-doped $NiTiO_3$/C was calculated to be the lowest, ~39 Ω, compared to $NiTiO_3$/C and Pt/C, suggesting faster kinetics for F-doped $NiTiO_3$/C in the OER. In terms of biomedical applications, F-doped $NiTiO_3$/C showed promising performance in removing Caco-2 cancer cells present in typical biomedical wastewater, as demonstrated by MTT cell viability assay, Caspases activation, DHE stain assay, MMP, Annexin/PI assays, and

fluorescence microscopy images. The IC50 concentration for this removal was found to be 0.15 μg/mL. The obtained results strongly suggest that carbonized F-doped $NiTiO_3$ photocatalysts can be quickly introduced as a promising candidates for multifunctional energy-environment applications.

Acknowledgment

The authors would like to acknowledge the support of Ajman University Internal Research Grant No. DGSR Ref. 2022-IRG-HBS-5. The authors are also grateful for the support of the NSFC (Grant Nos. 52161145409, 21976116) and INSF (Grant No. 4001153).

References

[1] O.A. Khaleel, D.S. Ahmed, Interface engineering at electron transport/perovskite layers using wetting mesoporous titanium dioxide to fabricate efficient and stable perovskite solar cells, International Journal of Energy Research, (2022).
[2] Q.-M. Fu, H.-K. Dong, W.-L. Li, H.-Y. Zhao, H. Tao, Z.-B. Ma, Y.-F. Tu, D. Zhou, Y. Tian, Effects of N Doping on Phase Transition and Visible-Light Photocatalytic Activity of ZnO/Zinc Titanate Core–Shell Nanorod Arrays, Journal of Electronic Materials, 51 (2022) 2599-2607.
[3] J. Zhang, W. Zhang, Y. Zhang, Polyethylene glycol-modified sol-gel synthesis of ZnTiO3 (n)-quartz composite microspheres for enhanced photocatalytic degradation of Reactive Brilliant Red X–3B, Ceramics International, 48 (2022) 28191-28198.
[4] L. Wang, P. Cai, Z. Liu, Z. Xie, Y. Fang, Role of carbon quantum dots on Nickel titanate to promote water oxidation reaction under visible light illumination, Journal of Colloid and Interface Science, 607 (2022) 203-209.
[5] E. Regulska, J. Breczko, A. Basa, Multifunctional NiTiO3-decorated-rGO nanostructure for energy storage, electro-and photocatalytic applications, Diamond and Related Materials, 128 (2022) 109310.
[6] B. Li, W. Wang, J. Zhao, Z. Wang, B. Su, Y. Hou, Z. Ding, W.-J. Ong, S. Wang, All-solid-state direct Z-scheme NiTiO 3/Cd 0.5 Zn 0.5 S heterostructures for photocatalytic hydrogen evolution with visible light, Journal of Materials Chemistry A, 9 (2021) 10270-10276.
[7] L. Wang, Y. Kong, Y. Fang, P. Cai, W. Lin, X. Wang, A Ga Doped NiTiO3 Photocatalyst for Overall Water Splitting under Visible Light Illumination, Advanced Functional Materials, 32 (2022) 2208101.
[8] A. Kramar, V. Anishchenko, P. Kuzema, N. Smirnova, I. Laguta, O. Stavinskaya, R. Ivannikov, O. Linnik, Photocatalytic activity of titania and iron titanates films in the process of lignin transformation, Ecological and environmental chemistry, 2022, pp. 69-70.
[9] N. Subha, M. Mahalakshmi, S. Monika, P.S. Kumar, V. Preethi, G. Vaishnavi, A. Rajabhuvaneswari, Heterostructured γ-Fe2O3/FeTiO3 magnetic nanocomposite: An efficient visible-light-driven photocatalyst for the degradation of organic dye, Chemosphere, 306 (2022) 135631.
[10] J. Niu, Y. Zhang, J. Shi, Z. Zhang, Z. Ma, B. Yao, X. Yu, X. Wang, Microwave-based preparation of γ-Fe2O3/SrTiO3 photocatalyst for efficient degradation of organic pollutants in water, Materials Chemistry and Physics, (2022) 126357.
[11] X. Zhang, Z. Li, B. Zeng, C. Li, H. Han, EPR study of charge separation associated states and reversibility of surface bound superoxide radicals in SrTiO3 photocatalyst, Journal of Energy

Chemistry, 70 (2022) 388-393.
[12] W. Zulfiqar, S.M. Alay-e-Abbas, Improved thermodynamic stability and visible light absorption in Zr+ X codoped (X= S, Se and Te) BaTiO3 photocatalysts: A first-principles study, Materials Today Communications, 32 (2022) 103867.
[13] A. Fazli, F. Zakeri, A. Khataee, Y. Orooji, A BaTiO3/WS2 composite for piezo-photocatalytic persulfate activation and ofloxacin degradation, Communications Chemistry, 5 (2022) 1-14.
[14] A.E. Maughan, A.M. Ganose, A.M. Candia, J.T. Granger, D.O. Scanlon, J.R. Neilson, Anharmonicity and octahedral tilting in hybrid vacancy-ordered double perovskites, Chemistry of Materials, 30 (2018) 472-483.
[15] L. Paramanik, S. Subudhi, K. Parida, Visible light active titanate perovskites: An overview on its synthesis, characterization and photocatalytic applications, Materials Research Bulletin, 155 (2022) 111965.
[16] S. Du, H. Zou, Y. Bao, Y. Qi, X. Xin, S. Wang, Z. Feng, F. Zhang, Homogeneous nitrogen-doped (111)-type layered Sr5Nb4O15− xNx as a visible-light-responsive photocatalyst for water oxidation, Nano Research, (2022) 1-9.
[17] B.-C. Chen, W.-H. Liao, C.-C. Wu, High-stability CsPbIBr2 nanocrystal with nitrogen-doped graphene quantum dot/titanium dioxide for enhancing rhodamine B photocatalytic degradation under visible light, Journal of Environmental Chemical Engineering, 10 (2022) 107534.
[18] X. Han, P. Liu, R. Ran, W. Wang, W. Zhou, Z. Shao, Non-metal fluorine doping in Ruddlesden–Popper perovskite oxide enables high-efficiency photocatalytic water splitting for hydrogen production, Materials Today Energy, 23 (2022) 100896.
[19] J. Wang, Y. Wang, Y. Wang, X. Zhang, Y. Fan, Y. Liu, Z. Yi, Role of P in improving V-doped SrTiO3 visible light photocatalytic activity for water splitting: A first–Principles study, International Journal of Hydrogen Energy, 46 (2021) 20492-20502.
[20] J. Wang, T. Wang, Z. Zhao, R. Wang, C. Wang, F. Zhou, S. Li, L. Zhao, M. Feng, Regulation of oxygen vacancies in SrTiO3 perovskite for efficient photocatalytic nitrogen fixation, Journal of Alloys and Compounds, 902 (2022) 163865.
[21] R. Hailili, Z.-Q. Wang, H. Ji, C. Chen, X.-Q. Gong, H. Sheng, J. Zhao, Mechanistic insights into the photocatalytic reduction of nitric oxide to nitrogen on oxygen-deficient quasi-two-dimensional bismuth-based perovskites, Environmental Science: Nano, 9 (2022) 1453-1465.
[22] M. Ismael, Enhanced photocatalytic hydrogen production and degradation of organic pollutants from Fe (III) doped TiO2 nanoparticles, Journal of Environmental Chemical Engineering, 8 (2020) 103676.
[23] M. Ismael, Highly effective ruthenium-doped TiO2 nanoparticles photocatalyst for visible-light-driven photocatalytic hydrogen production, New J. Chem., 43 (2019) 9596-9605.
[24] M. Ismael, A review and recent advances in solar-to-hydrogen energy conversion based on photocatalytic water splitting over doped-TiO2 nanoparticles, Solar Energy, 211 (2020) 522-546.
[25] H.L. Boström, G. Kieslich, Influence of metal defects on the mechanical properties of ABX3 perovskite-type metal-formate frameworks, The Journal of Physical Chemistry C, 125 (2021) 1467-1471.
[26] Z. Ma, Y. Wang, Y. Lu, H. Ning, J. Zhang, Tackling Challenges in Perovskite-Type Metal Oxide Photocatalysts, Energy Technology, 9 (2021) 2001019.
[27] R. Hailili, Z.-Q. Wang, X.-Q. Gong, C. Wang, Octahedral-shaped perovskite CaCu3Ti4O12 with dual defects and coexposed {(001),(111)} facets for visible-light photocatalysis, Applied Catalysis B: Environmental, 254 (2019) 86-97.
[28] N. Kitchamsetti, M. Samtham, P.N. Didwal, D. Kumar, D. Singh, S. Bimli, P.R. Chikate, D.A. Basha, S. Kumar, C.-J. Park, Theory abide experimental investigations on morphology driven enhancement of electrochemical energy storage performance for manganese titanate perovskites electrodes, Journal of Power Sources, 538 (2022) 231525.
[29] K. Fujinami, K. Katagiri, J. Kamiya, T. Hamanaka, K. Koumoto, Sub-10 nm strontium titanate nanocubes highly dispersed in non-polar organic solvents, Nanoscale, 2 (2010) 2080-2083.

[30] R. Djellabi, M.F. Ordonez, F. Conte, E. Falletta, C.L. Bianchi, I. Rossetti, A review of advances in multifunctional XTiO3 perovskite-type oxides as piezo-photocatalysts for environmental remediation and energy production, Journal of Hazardous Materials, 421 (2022) 126792.
[31] J. Wang, F. Zhang, Z. Peng, X. Chao, Z. Yang, Sodium bismuth titanate-based perovskite ceramics with high energy storage efficiency and discharge performance, Journal of Materiomics, (2022).
[32] W.-Y. Chen, C.-P. Wang, P.-C. Chen, K.-Y.A. Lin, S. Ghosh, C.-W. Huang, V.-H. Nguyen, Perovskite Zinc Titanate Photocatalysts Synthesized by the Sol–Gel Method and Their Application in the Photocatalytic Degradation of Emerging Contaminants, Catalysts, 11 (2021) 854.
[33] S. Selvarajan, P. Malathy, A. Suganthi, M. Rajarajan, Fabrication of mesoporous BaTiO3/SnO2 nanorods with highly enhanced photocatalytic degradation of organic pollutants, Journal of industrial and engineering chemistry, 53 (2017) 201-212.
[34] Y.H. Kim, Y. Kang, S. Jo, H. Jeong, D. Neagu, J.-h. Myung, Shape-shifting nanoparticles on a perovskite oxide for highly stable and active heterogeneous catalysis, Chemical Engineering Journal, 441 (2022) 136025.
[35] X. Chen, C.-C. Kou, X.-J. Liao, C.-X. Li, G.-J. Yang, K. Huang, C.-J. Li, Plasma-sprayed lanthanum-doped strontium titanate as an interconnect for solid oxide fuel cells: Effects of powder size and process conditions, Journal of Alloys and Compounds, 876 (2021) 160212.
[36] S. Noreen, A. Maqbool, I. Maqbool, A. Shafique, M.M. Khan, Y. Junejo, B. Ahmed, M. Anwar, A. Majeed, M. Abbas, Multifunctional mesoporous silica-based nanocomposites: Synthesis and biomedical applications, Materials Chemistry and Physics, 285 (2022) 126132.
[37] M. Ismael, E. Elhaddad, D.H. Taffa, M. Wark, Synthesis of phase pure hexagonal YFeO3 perovskite as efficient visible light active photocatalyst, Catalysts, 7 (2017) 326.
[38] M. Ismael, E. Elhaddad, D.H. Taffa, M. Wark, Solid state route for synthesis of YFeO3/g-C3N4 composites and its visible light activity for degradation of organic pollutants, Catalysis Today, 313 (2018) 47-54.
[39] M. Ismael, Y. Wu, A facile synthesis method for fabrication of LaFeO 3/gC 3 N 4 nanocomposite as efficient visible-light-driven photocatalyst for photodegradation of RhB and 4-CP, New J. Chem., 43 (2019) 13783-13793.
[40] M. Ismael, M. Wark, Perovskite-type LaFeO3: photoelectrochemical properties and photocatalytic degradation of organic pollutants under visible light irradiation, Catalysts, 9 (2019) 342.
[41] M. Ismael, Ferrites as solar photocatalytic materials and their activities in solar energy conversion and environmental protection: a review, Solar energy materials and solar cells, 219 (2021) 110786.
[42] A. Shawky, R. Mohamed, I. Mkhalid, M. Youssef, N. Awwad, Visible light-responsive Ag/LaTiO3 nanowire photocatalysts for efficient elimination of atrazine herbicide in water, Journal of Molecular Liquids, 299 (2020) 112163.
[43] S. Tu, H. Huang, T. Zhang, Y. Zhang, Controllable synthesis of multi-responsive ferroelectric layered perovskite-like Bi4Ti3O12: Photocatalysis and piezoelectric-catalysis and mechanism insight, Applied Catalysis B: Environmental, 219 (2017) 550-562.
[44] O. Jongprateep, N. Sato, R. Techapiesancharoenkij, K. Surawathanawises, P. Siwayaprahm, P. Watthanarat, Photocatalytic and antimicrobial activities of Sr x Ca (1-x) TiO 3 (x= 0, 0.25, 0.5, 0.75 and 1) powders synthesized by solution combustion technique, Journal of Metals, Materials and Minerals, 29 (2019).
[45] S. Cai, S. Yu, W. Wan, W. Wen, Y. Zhou, Self-template synthesis of ATiO 3 (A= Ba, Pb and Sr) perovskites for photocatalytic removal of NO, RSC advances, 7 (2017) 27397-27404.
[46] Y. Ma, Z. Zhao, Z. Shen, Q. Cai, H. Ji, L. Meng, Hydrothermal carbonation carbon-coated CdS nanocomposite with enhanced photocatalytic activity and stability, Catalysts, 7 (2017) 194.
[47] Q. Liang, G. Li, F. Rao, G. Zheng, H. Ma, S. Li, M. Hojamberdiev, Q. Wang, G. Zhu, Linking the enhanced deep NO oxidation of a ferroelectric K 0.5 Bi 0.5 TiO 3 nanowire photocatalyst to its spontaneous polarization and oxygen vacancies, Inorganic Chemistry Frontiers, 8 (2021) 5065-5075.

[48] M. Padervand, F. Nasiri, S. Hajiahmadi, A. Bargahi, S. Esmaeili, M. Amini, R.K. Nami, Z. Shahsavari, S. Karima, Ag@ Ag2MoO4 decorated polyoxomolybdate/C3N4 nanostructures as highly efficient photocatalysts for the wastewater treatment and cancer cells killing under visible light, Inorganic Chemistry Communications, 141 (2022) 109500.
[49] V.D. Dasireddy, B. Likozar, Photocatalytic CO2 reduction to methanol over bismuth promoted BaTiO3 perovskite nanoparticle catalysts, Renewable Energy, 195 (2022) 885-895.
[50] K. Tucki, R. Mruk, O. Orynycz, K. Botwińska, A. Gola, A. Bączyk, Toxicity of exhaust fumes (CO, NOx) of the compression-ignition (diesel) engine with the use of simulation, Sustainability, 11 (2019) 2188.
[51] G. Xie, N. Zhou, Y. Gao, S. Du, H. Du, J. Tao, L. Zhang, J. Zhu, On-demand release of CO2 from photothermal hydrogels for accelerating skin wound healing, Chemical Engineering Journal, 403 (2021) 126353.
[52] X. Wu, C. Wang, Y. Wei, J. Xiong, Y. Zhao, Z. Zhao, J. Liu, J. Li, Multifunctional photocatalysts of Pt-decorated 3DOM perovskite-type SrTiO3 with enhanced CO2 adsorption and photoelectron enrichment for selective CO2 reduction with H2O to CH4, Journal of Catalysis, 377 (2019) 309-321.
[53] S.-X. Yuan, K. Su, Y.-X. Feng, M. Zhang, T.-B. Lu, Lattice-matched in-situ construction of 2D/2D T-SrTiO3/CsPbBr3 heterostructure for efficient photocatalysis of CO2 reduction, Chinese Chemical Letters, (2022).
[54] S. Wan, M. Chen, M. Ou, Q. Zhong, Plasmonic Ag nanoparticles decorated SrTiO3 nanocubes for enhanced photocatalytic CO2 reduction and H2 evolution under visible light irradiation, Journal of CO2 Utilization, 33 (2019) 357-364.
[55] Q. Zhang, Y. Huang, S. Peng, Y. Zhang, Z. Shen, J.-j. Cao, W. Ho, S.C. Lee, D.Y. Pui, Perovskite LaFeO3-SrTiO3 composite for synergistically enhanced NO removal under visible light excitation, Applied Catalysis B: Environmental, 204 (2017) 346-357.
[56] J. Tang, R. Wang, M. Liu, Z. Zhang, Y. Song, S. Xue, Z. Zhao, D.D. Dionysiou, Construction of novel Z-scheme Ag/FeTiO3/Ag/BiFeO3 photocatalyst with enhanced visible-light-driven photocatalytic performance for degradation of norfloxacin, Chemical Engineering Journal, 351 (2018) 1056-1066.
[57] J. Wang, C. Xue, W. Yao, J. Liu, X. Gao, R. Zong, Z. Yang, W. Jin, D. Tao, MOF-derived hollow TiO2@ C/FeTiO3 nanoparticles as photoanodes with enhanced full spectrum light PEC activities, Applied Catalysis B: Environmental, 250 (2019) 369-381.
[58] J.E. Silveira, A.R. Ribeiro, J. Carbajo, G. Pliego, J.A. Zazo, J.A. Casas, The photocatalytic reduction of NO3− to N2 with ilmenite (FeTiO3): Effects of groundwater matrix, Water Research, 200 (2021) 117250.
[59] N.P. Zangeneh, S. Sharifnia, E. Karamian, Modification of photocatalytic property of BaTiO3 perovskite structure by Fe2O3 nanoparticles for CO2 reduction in gas phase, Environmental Science and Pollution Research, 27 (2020) 5912-5921.
[60] S.Y. Hwang, H.J. Jang, Y.J. Kim, J.Y. Maeng, C.K. Rhee, Y. Sohn, Eu (III)–BaTiO3 nanoparticles and BaTiO3/TiO2/Ti sheets; photocatalytic and electrocatalytic CO2 reduction, Materials Science in Semiconductor Processing, 153 (2023) 107134.
[61] X. Qin, J. Liu, Q. Zhang, W. Chen, X. Zhong, J. He, Synthesis of Yellow-Fluorescent Carbon Nano-dots by Microplasma for Imaging and Photocatalytic Inactivation of Cancer Cells, Nanoscale research letters, 16 (2021) 1-9.
[62] M. Padervand, S. Ghasemi, S. Hajiahmadi, B. Rhimi, Z.G. Nejad, S. Karima, Z. Shahsavari, C. Wang, Multifunctional Ag/AgCl/ZnTiO3 structures as highly efficient photocatalysts for the removal of nitrophenols, CO2 photoreduction, biomedical waste treatment, and bacteria inactivation, Applied Catalysis A: General, 643 (2022) 118794.
[63] K.R. Diab, H.H. El-Maghrabi, A.A. Nada, A.M. Youssef, A. Hamdy, S. Roualdes, S. Abd El-Wahab, Facile fabrication of NiTiO3/graphene nanocomposites for photocatalytic hydrogen generation, Journal of Photochemistry and Photobiology A: Chemistry, 365 (2018) 86-93.
[64] Y. Wang, X. Chen, Q. Wang, Y. Zeng, K. Liao, S. Zhang, Q. Zhong, Novel 3D hierarchical bifunctional NiTiO3 nanoflower for superior visible light photoreduction performance of CO2 to CH4

and high lithium storage performance, Energy, 169 (2019) 580-586.
[65] H. Guo, S. Wan, Y. Wang, W. Ma, Q. Zhong, J. Ding, Enhanced photocatalytic CO2 reduction over direct Z-scheme NiTiO3/g-C3N4 nanocomposite promoted by efficient interfacial charge transfer, Chemical Engineering Journal, 412 (2021) 128646.
[66] G. Li, Z. Lian, Z. Wan, Z. Liu, J. Qian, Y. Deng, S. Zhang, Q. Zhong, Ni (OH) 2 clusters decorated NiTiO3 Z-scheme heterojunctions with strong O2 activation and robust interfacial built-in electric field for efficient NO photo-oxidation, Chemical Engineering Journal, 451 (2023) 138625.
[67] M. Moniruddin, B. Ilyassov, X. Zhao, E. Smith, T. Serikov, N. Ibrayev, R. Asmatulu, N. Nuraje, Recent progress on perovskite materials in photovoltaic and water splitting applications, Materials Today Energy, 7 (2018) 246-259.
[68] N. Tanwar, S. Upadhyay, R. Priya, S. Pundir, P. Sharma, O. Pandey, Eu-doped BaTiO3 perovskite as an efficient electrocatalyst for oxygen evolution reaction, Journal of Solid State Chemistry, (2022) 123674.
[69] H.J. Jang, S.J. Park, J.H. Yang, S.-M. Hong, C.K. Rhee, D. Kim, Y. Sohn, Photocatalytic and photoelectrocatalytic properties of Eu (III)-doped perovskite SrTiO3 nanoparticles with dopant level approaches, Materials Science in Semiconductor Processing, 132 (2021) 105919.
[70] A. Hernández-Ramírez, M. Sánchez-Castro, I. Alonso-Lemus, K.K. Aruna, P. Karthikeyan, R. Manoharan, F. Rodríguez-Varela, Evaluation of the nickel titanate-modified Pt nanostructured catalyst for the ORR in alkaline media, Journal of The Electrochemical Society, 163 (2015) F16.
[71] J.M. Luque-Centeno, M. Martínez-Huerta, D. Sebastián, J.I. Pardo, M. Lázaro, CoTiO3/NrGO nanocomposites for oxygen evolution and oxygen reduction reactions: Synthesis and electrocatalytic performance, Electrochimica Acta, 331 (2020) 135396.
[72] V. Thiagarajan, P. Karthikeyan, R. Manoharan, S. Sampath, A. Hernández-Ramírez, M. Sánchez-Castro, I. Alonso-Lemus, F. Rodríguez-Varela, Pt-Ru-NiTiO3 nanoparticles dispersed on vulcan as high performance electrocatalysts for the methanol oxidation reaction (MOR), Electrocatalysis, 9 (2018) 582-592.
[73] K. Huo, Y. Li, R. Chen, B. Gao, C. Peng, W. Zhang, L. Hu, X. Zhang, P.K. Chu, Recyclable Non-Enzymatic Glucose Sensor Based on Ni/NiTiO3/TiO2 Nanotube Arrays, ChemPlusChem, 80 (2015) 576-582.
[74] V. Thiagarajan, R. Manoharan, P. Karthikeyan, E. Nikhila, A. Hernández-Ramírez, F. Rodriguez-Varela, Pt nanoparticles supported on NiTiO3/C as electrocatalyst towards high performance Methanol Oxidation Reaction, International Journal of Hydrogen Energy, 42 (2017) 9795-9805.
[75] Y. Li, G. Wang, Y. Wang, Z. Jin, Phosphating 2D CoAl LDH anchored on 3D self-assembled NiTiO 3 hollow rods for efficient hydrogen evolution, Catalysis Science & Technology, 10 (2020) 2931-2947.
[76] S. Hooshmand, S. Kargozar, A. Ghorbani, M. Darroudi, M. Keshavarz, F. Baino, H.-W. Kim, Biomedical waste management by using nanophotocatalysts: The need for new options, Materials, 13 (2020) 3511.
[77] M. Shajari, K. Rostamizadeh, R. Shapouri, L. Taghavi, Eco-friendly curcumin-loaded nanostructured lipid carrier as an efficient antibacterial for hospital wastewater treatment, Environmental Technology & Innovation, 18 (2020) 100703.
[78] M.M. Yallapu, S.F. Othman, E.T. Curtis, B.K. Gupta, M. Jaggi, S.C. Chauhan, Multi-functional magnetic nanoparticles for magnetic resonance imaging and cancer therapy, Biomaterials, 32 (2011) 1890-1905.
[79] X. Qi, X. Tong, W. Pan, Q. Zeng, S. You, J. Shen, Recent advances in polysaccharide-based adsorbents for wastewater treatment, Journal of Cleaner Production, 315 (2021) 128221.
[80] P. Sundaram, H. Abrahamse, Effective photodynamic therapy for colon cancer cells using chlorin e6 coated hyaluronic acid-based carbon nanotubes, International journal of molecular sciences, 21 (2020) 4745.
[81] Y. Ke, M.S. Al Aboody, W. Alturaiki, S.A. Alsagaby, F.A. Alfaiz, V.P. Veeraraghavan, S. Mickymaray, Photosynthesized gold nanoparticles from Catharanthus roseus induces caspase-mediated apoptosis in cervical cancer cells (HeLa), Artificial cells, nanomedicine, and biotechnology,

47 (2019) 1938-1946.
[82] J. Pilch, E. Matysiak-Brynda, A. Kowalczyk, P. Bujak, Z. Mazerska, A.M. Nowicka, E. Augustin, New unsymmetrical bisacridine derivatives noncovalently attached to quaternary quantum dots improve cancer therapy by enhancing cytotoxicity toward cancer cells and protecting normal cells, ACS applied materials & interfaces, 12 (2020) 17276-17289.
[83] M. Ismael, Photo-Fenton reaction enhanced visible-light activity of p- Photo-Fenton reaction enhanced visible-light activity of p-CuFe2O4/n-g-C3N4 heterojunction composites synthesized by a simple ultrasonic-assisted route for organic pollutants degradation, Materials Research Bulletin, 151 (2022) 111803.
[84] M. Ismael, M. Wark, Photocatalytic activity of CoFe2O4/g-C3N4 nanocomposite toward degradation of different organic pollutants and their inactivity toward hydrogen production: The role of the conduction band position, FlatChem, 32 (2022) 100337.
[85] X. Qi, R. Liu, M. Chen, Z. Li, T. Qin, Y. Qian, S. Zhao, M. Liu, Q. Zeng, J. Shen, Removal of copper ions from water using polysaccharide-constructed hydrogels, Carbohydrate Polymers, 209 (2019) 101-110.
[86] S. Dong, J. Feng, M. Fan, Y. Pi, L. Hu, X. Han, M. Liu, J. Sun, J. Sun, Recent developments in heterogeneous photocatalytic water treatment using visible light-responsive photocatalysts: a review, Rsc Advances, 5 (2015) 14610-14630.
[87] J. Lee, Y.H. Lee, J.S. Choi, K.S. Park, K.S. Chang, M. Yoon, Hydrothermal synthesis of defective TiO 2 nanoparticles for long-wavelength visible light-photocatalytic killing of cancer cells, RSC advances, 5 (2015) 99789-99796.
[88] M. Abdulla-Al-Mamun, Y. Kusumoto, T. Zannat, M.S. Islam, Synergistic enhanced photocatalytic and photothermal activity of Au@ TiO2 nanopellets against human epithelial carcinoma cells, Physical Chemistry Chemical Physics, 13 (2011) 21026-21034.
[89] M. Padervand, S. Hajiahmadi, Ag/AgCl@ Tubular g-C3N4 nanostructure as an enhanced visible light photocatalyst for the removal of organic dye compounds and biomedical waste under visible light, Journal of Photochemistry and Photobiology A: Chemistry, 425 (2022) 113700.
[90] B. He, H.-Y. Jin, Y.-W. Wang, C.-M. Fan, Y.-F. Wang, X.-C. Zhang, J.-X. Liu, R. Li, J.-W. Liu, Carbon quantum dots/Bi4O5Br2 photocatalyst with enhanced photodynamic therapy: killing of lung cancer (A549) cells in vitro, Rare Metals, 41 (2022) 132-143.
[91] R.A. AbuMousa, U. Baig, M.A. Gondal, M.A. Dastageer, M.S. AlSalhi, B. Moftah, F.Y. Alqahtani, S. Akhter, F.S. Aleanizy, Investigation of the survival viability of cervical cancer cells (HeLa) under visible light induced photo-catalysis with facile synthesized WO3/ZnO nanocomposite, Saudi journal of biological sciences, 27 (2020) 1743-1752.
[92] R.A. AbuMousa, U. Baig, M.A. Gondal, M.S. AlSalhi, F.Y. Alqahtani, S. Akhtar, F.S. Aleanizy, M.A. Dastageer, Photo-catalytic killing of HeLa cancer cells using facile synthesized pure and Ag loaded WO3 nanoparticles, Scientific reports, 8 (2018) 1-11.
[93] M. Padervand, S. Ghasemi, S. Hajiahmadi, C. Wang, K4Nb6O17/Fe3N/α-Fe2O3/C3N4 as an enhanced visible light-driven quaternary photocatalyst for acetamiprid photodegradation, CO2 reduction, and cancer cells treatment, Applied Surface Science, 544 (2021) 148939.
[94] Y. Qu, W. Zhou, Z. Ren, S. Du, X. Meng, G. Tian, K. Pan, G. Wang, H. Fu, Facile preparation of porous NiTiO 3 nanorods with enhanced visible-light-driven photocatalytic performance, Journal of Materials Chemistry, 22 (2012) 16471-16476.
[95] J.-L. Wang, Y.-Q. Li, Y.-J. Byon, S.-G. Mei, G.-L. Zhang, Synthesis and characterization of NiTiO3 yellow nano pigment with high solar radiation reflection efficiency, Powder Technology, 235 (2013) 303-306.
[96] K. Jurkiewicz, M. Pawlyta, A. Burian, Structure of carbon materials explored by local transmission electron microscopy and global powder diffraction probes, C, 4 (2018) 68.
[97] K. Lopes, L. Cavalcante, A.Z. Simões, J.A. Varela, E. Longo, E. Leite, NiTiO3 powders obtained by polymeric precursor method: Synthesis and characterization, Journal of alloys and compounds, 468 (2009) 327-332.

[98] W. Qi, A. Mattursun, M. Gao, A. Hushur, H. Zhang, Lattice dynamics of NiTiO3 under high pressure: Raman evidence under two pressure-transmitting mediums, Results in Physics, 43 (2022) 106114.
[99] S.K. Lakhera, H.Y. Hafeez, P. Veluswamy, V. Ganesh, A. Khan, H. Ikeda, B. Neppolian, Enhanced photocatalytic degradation and hydrogen production activity of in situ grown TiO2 coupled NiTiO3 nanocomposites, Applied Surface Science, 449 (2018) 790-798.
[100] S. Challagulla, K. Tarafder, R. Ganesan, S. Roy, Structure sensitive photocatalytic reduction of nitroarenes over TiO 2, Scientific reports, 7 (2017) 1-11.
[101] G. George, S. Anandhan, Synthesis and characterisation of nickel oxide nanofibre webs with alcohol sensing characteristics, RSC Advances, 4 (2014) 62009-62020.
[102] A. Sobhani-Nasab, Z. Zahraei, M. Akbari, M. Maddahfar, S.M. Hosseinpour-Mashkani, Synthesis, characterization, and antibacterial activities of ZnLaFe2O4/NiTiO3 nanocomposite, Journal of Molecular Structure, 1139 (2017) 430-435.
[103] V. Chellasamy, P. Thangadurai, Structural and electrochemical investigations of nanostructured NiTiO3 in acidic environment, Frontiers of Materials Science, 11 (2017) 162-170.
[104] J. Xiong, H. Zhong, J. Li, X. Zhang, J. Shi, W. Cai, K. Qu, C. Zhu, Z. Yang, S.P. Beckman, H. Cheng, Engineering highly active oxygen sites in perovskite oxides for stable and efficient oxygen evolution, Applied Catalysis B: Environmental, 256 (2019) 117817.
[105] V. Madurai Ramakrishnan, M. Natarajan, S. Pitchaiya, A. Santhanam, D. Velauthapillai, A. Pugazhendhi, Microwave assisted solvothermal synthesis of quasi cubic F doped TiO2 nanostructures and its performance as dye sensitized solar cell photoanode, International Journal of Energy Research, 45 (2021) 17259-17268.
[106] S. Zhang, Q. Zhong, W. Zhao, Y. Li, Surface characterization studies on F-doped V2O5/TiO2 catalyst for NO reduction with NH3 at low-temperature, Chemical Engineering Journal, 253 (2014) 207-216.
[107] Y. Zeng, Y. Wang, J. Chen, Y. Jiang, M. Kiani, B. Li, R. Wang, Fabrication of high-activity hybrid NiTiO3/g-C3N4 heterostructured photocatalysts for water splitting to enhanced hydrogen production, Ceramics International, 42 (2016) 12297-12305.
[108] J. Cheng, P. Liu, T. Peng, Q. Liu, W. Chen, B. Liu, Y. Yuan, W. Zhang, F. Song, J. Gu, Mechanically alloyed NiTiO 3/transition metal heterostructures: introducing oxygen vacancies for exceptionally enhanced hydrogen evolution reaction activity, Journal of Materials Chemistry A, 8 (2020) 14908-14914.
[109] Y. Li, J. Xu, M. Peng, Z. Liu, X. Li, S. Zhao, MoS2/NiTiO3 Heterojunctions as Photocatalysts: Improved Charge Separation for Promoting Photocatalytic Hydrogen Production Activity, Catalysis Surveys from Asia, 23 (2019) 277-289.
[110] P. Kaspar, D. Sobola, K. Částková, R. Dallaev, E. Šťastná, P. Sedlák, A. Knápek, T. Trčka, V. Holcman, Case study of polyvinylidene fluoride doping by carbon nanotubes, Materials, 14 (2021) 1428.
[111] T. Liu, A. Garsuch, F. Chesneau, B.L. Lucht, Surface phenomena of high energy Li (Ni1/3Co1/3Mn1/3) O2/graphite cells at high temperature and high cutoff voltages, Journal of Power Sources, 269 (2014) 920-926.
[112] C. Luo, J. Zhao, Y. Li, W. Zhao, Y. Zeng, C. Wang, Photocatalytic CO2 reduction over SrTiO3: Correlation between surface structure and activity, Applied Surface Science, 447 (2018) 627-635.
[113] H. Si, Y. Fang, L. Yang, Application of Supported TiO2 in Carbonated Binding Material and Its Photocatalytic Performance, Catalysts, 10 (2020) 1336.
[114] H. Chen, Z. Yang, C.L. Do-Thanh, S. Dai, What fluorine can do in CO2 chemistry: Applications from homogeneous to heterogeneous systems, ChemSusChem, 13 (2020) 6182-6200.
[115] G. Liu, A. Cadiau, Y. Liu, K. Adil, V. Chernikova, I.D. Carja, Y. Belmabkhout, M. Karunakaran, O. Shekhah, C. Zhang, Enabling fluorinated MOF-based membranes for simultaneous removal of H2S and CO2 from natural gas, Angewandte Chemie International Edition, 57 (2018) 14811-14816.
[116] W. Ni, Y. Xue, X. Zang, C. Li, H. Wang, Z. Yang, Y.-M. Yan, Fluorine doped cagelike carbon

electrocatalyst: an insight into the structure-enhanced CO selectivity for CO2 reduction at high overpotential, ACS nano, 14 (2020) 2014-2023.
[117] G. Wang, K. Leus, H.S. Jena, C. Krishnaraj, S. Zhao, H. Depauw, N. Tahir, Y.-Y. Liu, P. Van Der Voort, A fluorine-containing hydrophobic covalent triazine framework with excellent selective CO 2 capture performance, Journal of Materials Chemistry A, 6 (2018) 6370-6375.
[118] F. Li, X. Yue, L. Cheng, J. Fan, Q. Xiang, Hydrophobicity-aerophilicity effect boosting efficient CO2 photoreduction in graphitic carbon nitride modified with fluorine-containing groups, Chemical Engineering Journal, 452 (2023) 139463.
[119] C. Su, T. Yang, W. Zhou, W. Wang, X. Xu, Z. Shao, Pt/C–LiCoO 2 composites with ultralow Pt loadings as synergistic bifunctional electrocatalysts for oxygen reduction and evolution reactions, Journal of Materials Chemistry A, 4 (2016) 4516-4524.
[120] K. Kakaei, A. Rahimi, S. Husseindoost, M. Hamidi, H. Javan, A. Balavandi, Fabrication of Pt–CeO2 nanoparticles supported sulfonated reduced graphene oxide as an efficient electrocatalyst for ethanol oxidation, International Journal of Hydrogen Energy, 41 (2016) 3861-3869.
[121] K. Kakaei, M.D. Esrafili, A. Ehsani, Graphene surfaces: particles and catalysts, Academic Press2018.
[122] Z. Wei, S. Abbaspour, R. Tayebee, Nickel Nanoparticles Originated from Cressa Leaf Extract in the Preparation of a Novel Melem@ Ni-HPA Photocatalyst for the Synthesis of Some Chromenes and a Preliminary MTT Assay on the Anticancer Activity of the Nanocomposite, Polycyclic Aromatic Compounds, (2021) 1-20.
[123] Z. Sabouri, A. Akbari, H.A. Hosseini, M. Khatami, M. Darroudi, Tragacanth-mediate synthesis of NiO nanosheets for cytotoxicity and photocatalytic degradation of organic dyes, Bioprocess and biosystems engineering, 43 (2020) 1209-1218.
[124] M.A.J. Kouhbanani, Y. Sadeghipour, M. Sarani, E. Sefidgar, S. Ilkhani, A.M. Amani, N. Beheshtkhoo, The inhibitory role of synthesized Nickel oxide nanoparticles against Hep-G2, MCF-7, and HT-29 cell lines: the inhibitory role of NiO NPs against Hep-G2, MCF-7, and HT-29 cell lines, Green Chemistry Letters and Reviews, 14 (2021) 444-454.
[125] M. Ahamed, M.J. Akhtar, H.A. Alhadlaq, M.M. Khan, S.A. Alrokayan, Comparative cytotoxic response of nickel ferrite nanoparticles in human liver HepG2 and breast MFC-7 cancer cells, Chemosphere, 135 (2015) 278-288.
[126] K. Lingaraju, H.R. Naika, H. Nagabhushana, K. Jayanna, S. Devaraja, G. Nagaraju, Biosynthesis of nickel oxide nanoparticles from Euphorbia heterophylla (L.) and their biological application, Arabian Journal of Chemistry, 13 (2020) 4712-4719.
[127] K. Mohamed, K. Zine, K. Fahima, E. Abdelfattah, S.M. Sharifudin, K. Duduku, NiO nanoparticles induce cytotoxicity mediated through ROS generation and impairing the antioxidant defense in the human lung epithelial cells (A549): Preventive effect of Pistacia lentiscus essential oil, Toxicology reports, 5 (2018) 480-488.
[128] M. Hosseinkhah, R. Ghasemian, F. Shokrollahi, S.R. Mojdehi, M.J.S. Noveiri, M. Hedayati, M. Rezaei, A. Salehzadeh, Cytotoxic potential of nickel oxide nanoparticles functionalized with glutamic acid and conjugated with thiosemicarbazide (NiO@ Glu/TSC) against human gastric cancer cells, Journal of Cluster Science, 33 (2022) 2045-2053.
[129] T. Akar, A.S.Y. Saglam, P.U. Göçün, E. Alp, E. Konac, A. Menevşe, Evaluation of apoptotic caspase levels in estimation of the wound age, Turkish Journal of Biochemistry, 43 (2018) 126-133.
[130] S. Mrudhulla, A.K. Ravi, S. Muthukrishnan, V. Shanmugam, V.A. Arumugam, A. Muthukrishnan, Synthesis and Characterization of Nickel Nanoparticles of Gloriosa Superba and Its Anti-Angiogenic Activity in Cervical Cancer, (2022).
[131] H. Guo, H. Cui, J. Fang, Z. Zuo, J. Deng, X. Wang, L. Zhao, B. Wu, K. Chen, J. Deng, Nickel chloride-induced apoptosis via mitochondria-and Fas-mediated caspase-dependent pathways in broiler chickens, Oncotarget, 7 (2016) 79747.